RESEARCH ARTICLE

WILEY

# Anisotropic continuum framework of coupled gas flow – adsorption – deformation in sedimentary rocks

Qi Zhang[1]  |  Zhen-Yu Yin[1] 🆔  |  Xia Yan[2]

[1]Department of Civil and Environmental Engineering, The Hong Kong Polytechnic University, Hong Kong, China

[2]Research Center of Multiphase Flow in Porous Media, School of Petroleum Engineering, China University of Petroleum (East China), Qingdao, China

**Correspondence**
Zhen-Yu Yin, Department of Civil and Environmental Engineering, The Hong Kong Polytechnic University, Hung Hom, Kowloon, Hong Kong, 999077, China.
Email: zhenyu.yin@polyu.edu.hk

## Abstract

Solid deformation is always a crucial factor of gas transport in sedimentary rocks. While previous studies always adopt the assumption of isotropic poroelastic deformation, anisotropic poroelastoplastic deformation is rarely considered, despite anisotropy being a ubiquitous property of natural sedimentary rocks. In this work, an anisotropic poromechanical model is established to analyze the matrix porosity and apparent permeability evolutions during the process of gas migration. Using a thermodynamic formulation that treats the fluid–solid interface as an independent phase, we derive a rate form for matrix porosity and obtain the new dissipation function that contains three parts: dissipations from solid deformation, gas adsorption, and fluid flow. For gas adsorption, we justify the rationality of the adopted model; for fluid flow, the updated porosity can be substituted into sophisticated apparent permeability models for full-scale analysis; and for solid deformation, a recently developed constitutive model appropriate for rocks exhibiting transverse isotropy in both the elastic and plastic responses is adopted in this work. Through the novel stress-point simulation incorporating two effective stress measures and adsorption strain, new patterns of apparent permeability are obtained, which fit the experimental data quite well and cannot be reproduced from the assumption of isotropic poroelasticity. The advantages of our poromechanical model include thermodynamic consistency and the ability to employ finite-element-based formulation. Finally, an initial-boundary value problem of gas production considering anisotropic plasticity is conducted, and the effects of the bedding plane and different adsorption models are highlighted.

**KEYWORDS**
anisotropy, apparent permeability, elastoplasticity, poromechanics, shale gas

## 1 | INTRODUCTION

Energy markets around the world have been dramatically affected by the shale gas revolution in North America, making shale at the heart of energy resource development. Shale, the most common sedimentary rock on Earth, is estimated to

comprise 75% of rocks in sedimentary basins.[1] Whether it concerns geothermal energy,[2] carbon sequestration,[3] hydraulic fracturing,[4] underground mining,[5] or waste storage,[6] one is likely to encounter shale. Thus, knowing the deformation and fluid flow properties of shale is extremely important for the efficient exploration and utilization of natural resources. Similar to many natural and engineering materials, anisotropy is a ubiquitous property[7,8] due to the existence of distinct bedding planes.[9,10] The bedding plane (or layering) is the result of differences in settlement rates and source inputs during the sedimentation process.[11] Many plasticity models have been developed for anisotropic materials, see Borja et al.[12], Choo et al.[13], Crook et al.[14], Semnani et al.[15], Zhao et al.[16,17] for a sampling of these models. Nevertheless, none of these anisotropic plasticity models have been used in the shale gas community.

Darcy's law serves as a fundamental principle in numerous applications within the oil and gas sector.[18,19] However, it is only applicable to laminar and viscous flows, with deviations from this linear relationship termed as non-Darcy flow.[20] Shale is composed of an inorganic matrix with pore sizes ranging from 1 to 100 micrometers and an organic kerogen matrix with pore sizes between 1 to 200 nanometers.[21] For micrometer-sized pores, Darcy's law has proven to be suitable, but flow in nanometer pores often deviates from it, resulting in a non-Darcy flow. Wang and Sheng[22] noted that non-Darcy flow behaviors differ for gases and liquids. On one hand, for liquids, Darcy's law might overestimate flow rates due to fluid-particle interactions with solid pore walls.[22,23] Such interactions lead to the formation of a boundary layer where the liquid exhibits higher viscosity.[22,24] Consequently, the average fluid flow velocity is likely to be lower than the value derived from Darcy's law.[25,26] This phenomenon is referred to as low-velocity non-Darcy flow in literature.

Conversely, for gas flow in sedimentary rocks, several crucial mechanisms must be considered to accurately estimate realistic flow velocities. At the nanoscale, gas molecules are of similar size to the pores, and processes such as slippage at the pore walls, Knudsen diffusion, adsorption/desorption, and surface diffusion become significant.[21,27–29] Dynamic apparent permeability models are widely used to account for these non-Darcy flow mechanisms.[21,30–32] In these models, gas slippage at pore walls and Knudsen diffusion can be quantified using the Knudsen number $K_n$, which is the ratio of the mean free path of gas molecules to the pores' characteristic length.[33] At low $K_n$ ($K_n < 0.001$), almost all fluid molecules experience molecule-to-molecule interactions in the bulk fluid, and flow can be described as viscous flow (Darcy's law). As $K_n$ increases, molecule-to-wall interactions become significant and can no longer be neglected. Consequently, slip-flow occurs in the region $0.001 < K_n < 0.1$. Klinkenberg's equation and its modifications are effective in this slip-flow region. For $0.1 < K_n < 10$, flow is characterized in a transition region between slip-flow and free molecular flow. This region is particularly interesting since most shale reservoirs naturally fall within it, and it is also the most challenging region to model. When $K_n > 10$, flow is described as free molecular flow, which can be accurately modeled by molecular dynamics (MD), direct simulation Monte Carlo (DSMC), and Lattice-Boltzmann simulation.[34] In this study, the focus is on the region of $K_n < 10$.

Furthermore, adsorption/desorption processes[35] contribute to the formation of an adsorbed gas layer occupying pore space, causing variations in gas apparent permeability.[36] Additionally, stress sensitivity is another influential phenomenon that leads to changes in porosity and permeability.[37] As a result, the net change in permeability during gas extraction is controlled by multiple competing processes.[36] Numerous theoretical models have been developed to calculate apparent permeability and predict gas production.[38,39] Among the literature, Wang et al.[40] provided comprehensive overviews of multiscale and multiple gas transport/seepage mechanisms and proposed future research directions. Ip and Borja[41] captures the multiscale interactions of elastic anisotropy in unsaturated clay rocks through homogenization, and it mentions the distribution of nanopores impacts the gas transport and adsorption/desorption behavior,[41,42] which motivates the present study. However, despite extensive research on apparent permeability and related mechanisms, gas flow equations have not always been rigorously derived from poromechanics theory,[11,43–46] often adopting an uncoupled form that limits their applicability to anisotropic cases.

In this study, we present a novel framework for gas flow in sedimentary rocks experiencing both anisotropic elasto-plasticity and gas adsorption. Even though this study is motivated by shale properties, the discussion revolves around general sedimentary rocks whose characteristics are similar to those of shale. Inspired by Zhao and Borja[11] who focused on the slightly compressible fluid and constant permeability, we derive conservation laws of mass, momentum, and energy to include both adsorbed gas and free gas by using continuum principles of thermodynamics. A novel point simulation algorithm incorporating two effective stress measures and adsorption strain is developed for porosity and permeability updating. The paper is organized as follows. Section 2 and Section 3 mathematically formulate the problem in great detail. Section 4 conducts the stress-point simulation of the apparent permeability. An initial-boundary value problem of gas production considering anisotropic plasticity is conducted in Section 5, and the effects of the bedding plane and different adsorption models are highlighted.

## 2 | GOVERNING EQUATIONS

In this work, we follow the isothermal mixture theory formulations.[47–50] We assume all the connected pores are filled with gas, the solid is made of a single mineral, and it does not contain any occluded pores.[51] The effects of the residual/irreducible saturation of the liquid phase at the solid boundary are negligible.

Motivated by the three-phase approach originally developed by Zhang,[49] we model the fluid–solid interface as the third phase in mixture theory. We assume that the surface moves together with the solid skeleton, i.e., they have the same velocity. In terms of the notation, we still use the subscript or superscript "$f$" to represent the gas phase for the following two reasons. First, gas definitely belongs to one type of fluid. Second, we want to derive the formulation considering the most general cases, which implies our approach is also applicable to other types of fluids, and we will only reduce our formulation for the case of gas in Section 3.

### 2.1 | Mass balance

Considering mass exchange between the interface and the pore fluid, the individual mass balance equations in the current configuration could be written as

$$\frac{d\rho^s}{dt} + \rho^s \nabla \cdot \boldsymbol{v}_s = 0 \,, \tag{1}$$

$$\frac{d^f \rho^f}{dt} + \rho^f \nabla \cdot \boldsymbol{v}_f + \hat{r} = 0 \,, \tag{2}$$

$$\frac{d(\rho_{\text{surf}} A_s)}{dt} + \rho_{\text{surf}} A_s \nabla \cdot \boldsymbol{v}_s - \hat{r} = 0 \,, \tag{3}$$

where $\rho^s = \rho_s(1 - \phi)$ and $\rho^f = \rho_f \phi$ (with superscript) are partial densities of the solid and fluid, $\rho_s$ and $\rho_f$ (with subscript) are intrinsic densities, and $\phi$ is the porosity ($1 - \phi$ could be viewed as the solid porosity[48]). For the time derivative in the above three equations, $d/dt$ implies the material time derivative following the solid motion, while $d^f/dt$ follows the fluid motion, and they are related to the solid velocity $\boldsymbol{v}_s$ and fluid interstitial velocity $\boldsymbol{v}_f$, respectively. For the new mass balance equation of the interface, $A_s$ plays a similar role to $\phi$ but has a different dimension, it represents the amount of interface area per unit of current control volume,[49] simply known as the specific surface area. Similarly, $\rho_{\text{surf}}$ plays the role of intrinsic surface fluid density and therefore, $\rho_{\text{surf}} A_s$ has the same unit as $\rho^s$ and $\rho^f$. Finally, $\hat{r}$ measures the rate of adsorption by mass.

For the following algebraic simplifications, it is beneficial to express Equations 2, 3 by using some Lagrangian quantities and relative seepage velocity as

$$\frac{d\left(\rho_f \phi_L\right)}{dt} + J \nabla \cdot \hat{\boldsymbol{w}}_f + J\hat{r} = 0 \,, \tag{4}$$

$$\frac{d\left(\rho_{\text{surf}} \bar{A}_s\right)}{dt} = J\hat{r} \,, \tag{5}$$

where $\phi_L = J\phi$ is the Lagrangian porosity (the amount of pore space per unit of reference control volume) and $\bar{A}_s = JA_s$ is the Lagrangian specific surface area. In these two definitions, the important term $J$ is known as deformation Jacobian that measures the volume change during deformation, and it has an important property such that $dJ/dt = J \nabla \cdot \boldsymbol{v}_s$. Finally, $\hat{\boldsymbol{w}}_f = \rho_f \phi(\boldsymbol{v}_f - \boldsymbol{v}_s)$ is the Eulerian relative mass flux vector. Note that the symbol $\nabla$ always implies spatial derivative with respect to the current configuration.

### 2.2 | Momentum balance

The balance of linear momentum states that (assuming quasi-static condition throughout the paper)

$$\nabla \cdot \boldsymbol{\sigma}^s + \rho^s \boldsymbol{g} + \boldsymbol{h}^s = \boldsymbol{0} \,, \tag{6}$$

$$\nabla \cdot \boldsymbol{\sigma}^f + \rho^f \boldsymbol{g} + \boldsymbol{h}^f = -\hat{r}\boldsymbol{v}_f \,, \tag{7}$$

$$\nabla \cdot \boldsymbol{\sigma}^{\mathrm{surf}} + \rho_{\mathrm{surf}} A_s \boldsymbol{g} + \boldsymbol{h}^{\mathrm{surf}} = \hat{r}\boldsymbol{v}_s \,, \tag{8}$$

where $\boldsymbol{\sigma}^\alpha$ ($\alpha = s, f, \mathrm{surf}$) denotes the partial stress tensor of each phase, $\boldsymbol{g}$ is the gravity acceleration vector, and $\boldsymbol{h}^\alpha$ denotes the dragging force (Zhang[49] interpreted it as the linear momentum exchange among phases) and satisfies $\sum_\alpha \boldsymbol{h}^\alpha = \boldsymbol{0}$. Summation of the above three equations gives the overall balance of linear momentum as

$$\nabla \cdot \boldsymbol{\sigma} + \left(\rho^s + \rho^f + \rho_{\mathrm{surf}} A_s\right)\boldsymbol{g} + \hat{r}\tilde{\boldsymbol{v}}_f = \boldsymbol{0}\,, \tag{9}$$

where $\boldsymbol{\sigma} = \boldsymbol{\sigma}^s + \boldsymbol{\sigma}^f + \boldsymbol{\sigma}^{\mathrm{surf}}$ is the total Cauchy stress tensor and $\tilde{\boldsymbol{v}}_f$ is defined as $\tilde{\boldsymbol{v}}_f = \boldsymbol{v}_f - \boldsymbol{v}_s$. By using $\tilde{\boldsymbol{v}}_f$, $\hat{\boldsymbol{w}}_f$ could also be represented as $\hat{\boldsymbol{w}}_f = \rho_f \phi \tilde{\boldsymbol{v}}_f$.

It is worth noting that Equation 9 implies the mass transfer $\hat{r}$ affects the variation of the overall linear momentum, which is supported by similar equations in Choo and Borja[52], Choo et al.[53], Coussy[54], Zhao and Borja[11] for double porosity media. However, in Zhang,[49] the overall balance of linear momentum takes the same form as the usual porous media (without the $\hat{r}\tilde{\boldsymbol{v}}_f$ term). This difference comes from the treatment of the linear momentum balance for each phase: the term on the right-hand side (RHS) of Equations 7, 8 is a direct result of the Reynolds transport theorem[55]; while Zhang[49] added **the same one** on the left-hand side (LHS), in order to cancel out this RHS term. In our study, we do not choose to add such a term, which is consistent with our previous treatment in double porosity media, see Zhang et al.[56] Similar issues also exist in the energy balance as shown below, but we will state our assumptions clearly beforehand.

## 2.3 | Energy balance: The first law of thermodynamics

Let $\mathcal{K}$ be the kinetic energy and $\mathcal{I}$ be the internal energy of the whole material. The first law of thermodynamics states that

$$\frac{\mathrm{D}\mathcal{I}}{\mathrm{D}t} = \mathcal{P} - \frac{\mathrm{D}\mathcal{K}}{\mathrm{D}t}\,, \tag{10}$$

where $\mathcal{P}$ is the total power and the symbol $\mathrm{D}(\cdot)/\mathrm{D}t$ denotes the total material time derivative, which is obtained as the sum of the material time derivatives for each phase. By using the Reynolds transport theorem,[55] the time derivative of kinetic energy could be expressed as

$$\frac{\mathrm{D}\mathcal{K}}{\mathrm{D}t} = \int_{\Omega(t)} \frac{\hat{r}}{2}\left(\|\boldsymbol{v}_s\|^2 - \|\boldsymbol{v}_f\|^2\right)\mathrm{d}V_t\,, \tag{11}$$

where $\Omega(t)$ implies the current configuration. Note for the dynamic case, Equation 11 should incorporate acceleration terms. For the power term, by using the Gauss divergence theorem, it could be derived as

$$\mathcal{P} = \int_{\Omega(t)} \left\{ \boldsymbol{\sigma} : \boldsymbol{d} - p\phi\nabla \cdot \tilde{\boldsymbol{v}}_f + \hat{r}\left(\|\boldsymbol{v}_s\|^2 - \|\boldsymbol{v}_f\|^2\right) - \boldsymbol{h}^f \cdot \tilde{\boldsymbol{v}}_f \right\}\mathrm{d}V_t\,, \tag{12}$$

where $\boldsymbol{d}$ is the rate of deformation tensor, $p$ is the pore fluid pressure and it emanates from the assumption on the form of $\boldsymbol{\sigma}^f$, that is, $\boldsymbol{\sigma}^f = -\phi p\boldsymbol{1}$ where $\boldsymbol{1}$ is the second-order identity tensor, and this form suggests the isotropic characteristic of the fluid pressure. Note in the evaluation of $\mathcal{P}$, we only consider the power of the surface forces and gravity forces,[43,54] in other words, the power done by dragging force and mass transfer $\hat{r}$ is not involved. This is emphasized in Coussy[54] and we thus follow this recipe, and it could lead to differences with the formulation of Zhang.[49] In order to further simplify Equation 12, we could solve for $\boldsymbol{h}^f$ from Equation 7 and substitute it into Equation 12. After some algebraic manipulations, we obtain

$$\mathcal{P} - \frac{\mathrm{D}\mathcal{K}}{\mathrm{D}t} = \int_{\Omega(t)} \left\{ \boldsymbol{\sigma} : \boldsymbol{d} - \nabla \cdot \left(\frac{p}{\rho_f}\hat{\boldsymbol{w}}_f\right) + \boldsymbol{g} \cdot \hat{\boldsymbol{w}}_f + \frac{\hat{r}}{2}\|\tilde{\boldsymbol{v}}_f\|^2 \right\}\mathrm{d}V_t\,. \tag{13}$$

Now we work on the time derivative of internal energy $\mathcal{I}$. We define the overall internal energy per unit current volume $e$ to be

$$e = \rho^s \hat{e}_s + \rho^f \hat{e}_f + \rho_{\mathrm{surf}} A_s \hat{e}_{\mathrm{surf}}, \tag{14}$$

where $\hat{e}_\alpha$ represents the mass-specific (i.e., per mass unit) internal energy of each phase.[50] By using the deformation Jacobian $J$, we also define the Lagrangian counterpart $E$ as $E = Je$, which represents the overall internal energy per unit reference volume.[50] The LHS of Equation 10 can be represented as

$$\frac{\mathrm{D}\mathcal{I}}{\mathrm{D}t} = \frac{\mathrm{d}}{\mathrm{d}t}\int_{\Omega(t)} (\rho^s \hat{e}_s + \rho_{\mathrm{surf}} A_s \hat{e}_{\mathrm{surf}})\, \mathrm{d}V_t + \frac{\mathrm{d}^f}{\mathrm{d}t}\int_{\Omega(t)} \rho^f \hat{e}_f\, \mathrm{d}V_t, \tag{15}$$

which could be simplified into the following more compact form

$$\frac{\mathrm{D}\mathcal{I}}{\mathrm{D}t} = \int_{\Omega(t)} \left\{ \frac{\mathrm{d}e}{\mathrm{d}t} + e\nabla \cdot \boldsymbol{v}_s + \nabla \cdot \left( \hat{e}_f \hat{\boldsymbol{w}}_f \right) \right\} \mathrm{d}V_t. \tag{16}$$

Note this is the most complete result for the rate of overall internal energy. The results derived in Borja[48], Zhang et al.[56], Zhao and Borja[11] are approximate results that only consider the first term. By combining Equation 13 and Equation 16, we obtain the energy balance equation in the current configuration as

$$\frac{\mathrm{d}e}{\mathrm{d}t} + e\nabla \cdot \boldsymbol{v}_s = \boldsymbol{\sigma} : \boldsymbol{d} - \nabla \cdot \left( \hat{h}_f \hat{\boldsymbol{w}}_f \right) + \boldsymbol{g} \cdot \hat{\boldsymbol{w}}_f + \frac{\hat{r}}{2}\left\| \tilde{\boldsymbol{v}}_f \right\|^2, \tag{17}$$

where we define $\hat{h}_f = \hat{e}_f + p/\rho_f$ as the mass-specific enthalpy.[49,54] We can also express the above equation using $E$ as

$$\frac{\mathrm{d}E}{\mathrm{d}t} = \boldsymbol{\tau} : \boldsymbol{d} - J\nabla \cdot \left( \hat{h}_f \hat{\boldsymbol{w}}_f \right) + J\boldsymbol{g} \cdot \hat{\boldsymbol{w}}_f + \frac{J\hat{r}}{2}\left\| \tilde{\boldsymbol{v}}_f \right\|^2, \tag{18}$$

where $\boldsymbol{\tau} = J\boldsymbol{\sigma}$ is known as the Kirchoff stress tensor.[55]

## 2.4 | Entropy inequality: The second law of thermodynamics

We can do exactly the same thing to the overall entropy, and define the Eulerian quantity $s$ and Lagrangian counterpart quantity $S = Js$. The (isothermal) second law of thermodynamics (entropy inequality) states that

$$\frac{\mathrm{d}S}{\mathrm{d}t} + J\nabla \cdot \left( \hat{s}_f \hat{\boldsymbol{w}}_f \right) = \frac{\Phi_L}{T} \geq 0, \tag{19}$$

where according to Equation 14, $\hat{s}_f$ could be inferred as the mass-specific fluid entropy, $T$ is temperature, which is treated as a positive constant, and $\Phi_L$ is the total dissipation per unit reference volume.

Now we introduce the overall Lagrangian density of Helmholtz free energy $\Psi = E - TS$ and take time derivatives on both sides, we obtain

$$T\frac{\mathrm{d}S}{\mathrm{d}t} = \frac{\mathrm{d}E}{\mathrm{d}t} - \frac{\mathrm{d}\Psi}{\mathrm{d}t}. \tag{20}$$

Since we have provided the expression of $\mathrm{d}E/\mathrm{d}t$ in Equation 18, we could combine with Equation 20 to get

$$\Phi_L = \boldsymbol{\tau} : \boldsymbol{d} + J\left[ \boldsymbol{g} \cdot \hat{\boldsymbol{w}}_f + \frac{\hat{r}}{2}\left\| \tilde{\boldsymbol{v}}_f \right\|^2 - \nabla \cdot \left( \hat{g}_f \hat{\boldsymbol{w}}_f \right) \right] - \frac{\mathrm{d}}{\mathrm{d}t}\left( J\rho^s \hat{\psi}_s + \rho_{\mathrm{surf}} \bar{A}_s \hat{\psi}_{\mathrm{surf}} + \rho_f \phi_L \hat{\psi}_f \right) \geq 0, \tag{21}$$

where $\hat{g}_f = \hat{h}_f - T\hat{s}_f$ is known as the mass-specific Gibbs potential and we have decomposed the overall $\Psi$ into three parts, that is, free energy stored in solid, fluid-solid interface, and the fluid itself. $\hat{\psi}_\alpha$ represents the mass-specific Helmholtz free energy and $\hat{\psi}_f$ is related to $\hat{g}_f$ through $\hat{\psi}_f = \hat{g}_f - p/\rho_f$.

Before continuing the simplification, we need to review the fluid state equations.[50,54] So far, we have introduced many mass-specific fluid quantities such as $\hat{g}_f$ and $\hat{\psi}_f$. They depend on the fluid pressure $p$, fluid density $\rho_f$, mass-specific fluid entropy $\hat{s}_f$, and temperature $T$. For $\hat{g}_f$, we choose $p$ and $T$ to be the complete set of independent thermodynamical state variables, and the dependent conjugate set is $1/\rho_f$ and $\hat{s}_f$. The two sets are related by

$$\mathrm{d}\hat{g}_f = \frac{1}{\rho_f}\mathrm{d}p - \underbrace{\hat{s}_f\,\mathrm{d}T}_{=0}\,. \tag{22}$$

While for $\hat{\psi}_f$, $1/\rho_f$ and $T$ are chose as the independent set, which is related to $p$ and $\hat{s}_f$ through

$$\mathrm{d}\hat{\psi}_f = -p\,\mathrm{d}\left(\frac{1}{\rho_f}\right) - \underbrace{\hat{s}_f\,\mathrm{d}T}_{=0}\,. \tag{23}$$

In Appendix A, we provide the specific form of $\hat{g}_f$ and $\hat{\psi}_f$ for an ideal monoatomic gas (e.g., He, Ne, Ar, Kr, Xe, and Rn), so one can use them to verify the above two state Equations 22 and 23.

By using Equations 22, 23 and the mass balance equations, we could finally simplify Equation 21 as

$$\Phi_L = \underbrace{\boldsymbol{\tau} : \boldsymbol{d} + p\frac{\mathrm{d}\phi_L}{\mathrm{d}t} - J\rho^s\frac{\mathrm{d}\hat{\psi}_s}{\mathrm{d}t} - \rho_{\mathrm{surf}}\bar{A}_s\frac{\mathrm{d}\hat{\psi}_{\mathrm{surf}}}{\mathrm{d}t} + J\hat{r}\left[\hat{g}_f + \frac{1}{2}\left\|\tilde{\boldsymbol{v}}_f\right\|^2 - \hat{\psi}_{\mathrm{surf}}\right]}_{\Phi_M^s + \Phi_M^{ad}}$$

$$+\underbrace{J\left(-\nabla p + \rho_f\boldsymbol{g}\right)\cdot\frac{\hat{\boldsymbol{w}}_f}{\rho_f}}_{\Phi_f} \geq 0\,, \tag{24}$$

where we split the total dissipation $\Phi_L$ into three parts, which represent dissipations from solid deformation $\Phi_M^s$, gas adsorption $\Phi_M^{ad}$, and fluid flow $\Phi_f$.

In order to evaluate the dissipation from solid deformation $\Phi_M^s$, we need to work on the $\mathrm{d}\phi_L/\mathrm{d}t$ term, that is, the porosity evolution. Therefore, in Section 2.5 and Section 2.6, we first derive the porosity evolution equation and reduced dissipation, and then in Section 3, the specific constitutive laws will be specified.

## 2.5 | Porosity evolution equation

The porosity evolution starts from the mass balance of the solid (Equation 1), while during the derivation, some assumptions are needed, which are summarized in the following bullet form:

1. Only infinitesimal deformation is considered. Therefore, the infinitesimal strain tensor $\boldsymbol{\epsilon} = \nabla^{\mathrm{sym}}\boldsymbol{u}$ is applicable where $\nabla^{\mathrm{sym}}$ is the symmetric gradient operator and $\boldsymbol{u}$ is the displacement.
2. The infinitesimal strain $\boldsymbol{\epsilon}$ is expressed as the sum of elastic strain $\boldsymbol{\epsilon}^e$, plastic strain $\boldsymbol{\epsilon}^p$, and adsorption strain $\boldsymbol{\epsilon}^{ad}$. The mechanical strain only contains $\boldsymbol{\epsilon}^e$ and $\boldsymbol{\epsilon}^p$. This is analogous to the thermo-poromechanics.
3. For elastic strain $\boldsymbol{\epsilon}^e$, by making an analogy between the adsorption strain and thermal strain,[57,58] we assume $\bar{\boldsymbol{\sigma}} = \boldsymbol{\sigma} + \boldsymbol{\alpha}p = \mathbb{C}^e : \boldsymbol{\epsilon}^e$ is still valid, where $\mathbb{C}^e$ is the fourth-order elastic tensor, $\boldsymbol{\alpha}$ is the Biot coefficient tensor,[59] and $\bar{\boldsymbol{\sigma}}$ is denoted as the Biot effective stress (note that $\boldsymbol{\sigma}'$ is reserved for other use). In other words, if we express the poroelastic relation in terms of purely mechanical strain and effective stress, the form will be identical to that of the "standard" porous media.[60–62]
4. The time derivative of $\sigma_m^{\mathrm{surf}} = \mathrm{Tr}(\boldsymbol{\sigma}^{\mathrm{surf}})/3$ introduced in Equation 8 is much smaller (in magnitude) than the solid grain bulk modulus $K_s$, i.e., we assume $1/K_s \times \mathrm{d}\sigma_m^{\mathrm{surf}}/\mathrm{d}t \approx 0$.

According to the definition of $K_s$ given by Borja[48]

$$K_s = \rho_s\frac{\mathrm{d}p_s}{\mathrm{d}\rho_s}\,, \tag{25}$$

where $p_s$ is the intrinsic solid pressure (positive for compression), Equation 1 can be simplified to

$$\frac{1-\phi}{K_s}\frac{dp_s}{dt} - \frac{d\phi}{dt} + (1-\phi)\nabla \cdot \boldsymbol{v}_s = 0. \tag{26}$$

Then by using the fact that $\boldsymbol{\sigma} = \boldsymbol{\sigma}^s + (-\phi p\mathbf{1}) + \boldsymbol{\sigma}^{\text{surf}}$ and $\text{Tr}(\boldsymbol{\sigma}^s)/3 = -(1-\phi)p_s$, Equation 26 can be further simplified to eliminate $dp_s/dt$ as

$$\left(1 + \frac{p-p_s}{K_s}\right)\frac{d\phi}{dt} = (1-\phi)\nabla \cdot \boldsymbol{v}_s - \frac{1}{K_s}\left(\frac{d\sigma_t}{dt} - \frac{d\sigma_m^{\text{surf}}}{dt} + \phi\frac{dp}{dt}\right), \tag{27}$$

where $\sigma_t = \text{Tr}(\boldsymbol{\sigma})/3$ is the mean total stress. To further eliminate $d\sigma_t/dt$, we make use of assumption 3, which yields

$$\frac{\mathbf{1}:\mathbb{C}^e}{3}:\frac{d\epsilon^e}{dt} = \frac{d\sigma_t}{dt} + \frac{\boldsymbol{\alpha}:\mathbf{1}}{3}\frac{dp}{dt}. \tag{28}$$

We next substitute Equation 28 into Equation 27 and ignore the $d\sigma_m^{\text{surf}}/dt$ term according to assumption 4, and the result reads

$$\left(1 + \frac{p-p_s}{K_s}\right)\frac{d\phi}{dt} = (1-\phi)\nabla \cdot \boldsymbol{v}_s - \frac{\mathbf{1}:\mathbb{C}^e}{3K_s}:\frac{d\epsilon^e}{dt} + \frac{1}{K_s}\left(\frac{\boldsymbol{\alpha}:\mathbf{1}}{3} - \phi\right)\frac{dp}{dt}. \tag{29}$$

We note that $(p-p_s)/K_s$ is on the order of strain, which should be much less than 1 for infinitesimal deformation.[11] As a result, we could ignore this term and further simplify Equation 29 by using assumption 2, we obtain

$$\frac{d\phi}{dt} = (\boldsymbol{\alpha} - \phi\mathbf{1}):\frac{d\epsilon^e}{dt} + (\mathbf{1} - \phi\mathbf{1}):\frac{d\epsilon^p}{dt} + (\mathbf{1} - \phi\mathbf{1}):\frac{d\epsilon^{ad}}{dt} + \frac{1}{K_s}\left(\frac{\boldsymbol{\alpha}:\mathbf{1}}{3} - \phi\right)\frac{dp}{dt}. \tag{30}$$

A simple implicit backward integration leads to

$$\phi = \frac{\boldsymbol{\alpha}:(\epsilon^e - \epsilon_n^e) + \mathbf{1}:(\epsilon^p - \epsilon_n^p) + \mathbf{1}:(\epsilon^{ad} - \epsilon_n^{ad}) + \frac{(\boldsymbol{\alpha}:\mathbf{1})(p - p_n)}{3K_s} + \phi_n}{1 + (\epsilon_v - \epsilon_{v,n}) + \frac{p - p_n}{K_s}}, \tag{31}$$

where the quantities with subscript "n" (in normal font) simply imply their values at the previous time step. For a better comparison, the porosity evolution equation emanated from poroelasticity theory is derived in Appendix B, which confirms the correctness of Equation 31. In addition, Equation 31 could also be recast into other prototypes of porosity evolution,[49,60,62] which confirms the generalizability of Equation 31.

We can rewrite Equation 30 by using Lagrangain porosity $\phi_L$, which is given as

$$\frac{1}{J}\frac{d\phi_L}{dt} = \boldsymbol{\alpha}:\frac{d\epsilon^e}{dt} + \mathbf{1}:\frac{d\epsilon^p}{dt} + \mathbf{1}:\frac{d\epsilon^{ad}}{dt} + \frac{1}{K_s}\left(\frac{\boldsymbol{\alpha}:\mathbf{1}}{3} - \phi\right)\frac{dp}{dt}. \tag{32}$$

Now we could substitute the above equation into Equation 24 and obtain an equivalent form as

$$\Phi = \frac{\Phi_L}{J} = \bar{\boldsymbol{\sigma}}:\frac{d\epsilon^e}{dt} + (\boldsymbol{\sigma} + p\mathbf{1}):\frac{d\epsilon^p}{dt} + \frac{p}{K_s}\left(\frac{\boldsymbol{\alpha}:\mathbf{1}}{3} - \phi\right)\frac{dp}{dt} - \rho^s\frac{d\hat{\psi}_s}{dt}$$

$$+ (\boldsymbol{\sigma} + p\mathbf{1}):\frac{d\epsilon^{ad}}{dt} - \rho_{\text{surf}}A_s\frac{d\hat{\psi}_{\text{surf}}}{dt} + \hat{r}\left[\hat{g}_f + \frac{1}{2}\left\|\tilde{\boldsymbol{v}}_f\right\|^2 - \hat{\psi}_{\text{surf}}\right]$$

$$+ (-\nabla p + \rho_f\boldsymbol{g})\cdot\frac{\hat{\boldsymbol{w}}_f}{\rho_f}, \tag{33}$$

where we have already made the small strain approximation such that the rate of deformation tensor $\boldsymbol{d}$ can be approximated by $d\epsilon/dt$.[54]

## 2.6 | Reduced dissipation

As a final preclude to the constitutive modeling in Section 3, we will derive the reduced dissipation from Equation 33. We assume the mass-specific free energy of solid $\hat{\psi}_s$ has an additive form of a "recoverable energy" part and a "trapped energy" part, and $\hat{\psi}_s$ is a function of the following variables

$$\hat{\psi}_s = \hat{\psi}_s\left(\epsilon^e, p, \boldsymbol{\xi}^p\right), \tag{34}$$

where $\epsilon^e$ and $p$ belong to the "recoverable" part, and $\boldsymbol{\xi}^p$ is a vector of strain-like plastic internal variables that belongs to the "trapped energy" part. By substituting Equation 34 into Equation 33 and using the standard Coleman argument, we get the following relations

$$\bar{\boldsymbol{\sigma}} = \rho^s \frac{\partial \hat{\psi}_s}{\partial \epsilon^e}, \qquad \frac{p}{K_s}\left(\frac{\boldsymbol{\alpha}:\mathbf{1}}{3} - \phi\right) = \rho^s \frac{\partial \hat{\psi}_s}{\partial p}. \tag{35}$$

Note the first relation is exactly the elastic functional relation between the Biot effective stress $\bar{\boldsymbol{\sigma}}$ and solid skeleton elastic strain $\epsilon^e$. The reduced dissipation $\mathcal{D}$ simplified from $\Phi$ now takes the form

$$
\begin{aligned}
\mathcal{D} = {} & (\boldsymbol{\sigma} + p\mathbf{1}) : \frac{\mathrm{d}\epsilon^p}{\mathrm{d}t} + \boldsymbol{\chi} \cdot \frac{\mathrm{d}\boldsymbol{\xi}^p}{\mathrm{d}t} \\
& + (\boldsymbol{\sigma} + p\mathbf{1}) : \frac{\mathrm{d}\epsilon^{ad}}{\mathrm{d}t} - \rho_{\mathrm{surf}} A_s \frac{\mathrm{d}\hat{\psi}_{\mathrm{surf}}}{\mathrm{d}t} + \hat{r}\left[\hat{g}_f + \frac{1}{2}\left\|\tilde{\boldsymbol{v}}_f\right\|^2 - \hat{\psi}_{\mathrm{surf}}\right] \\
& + \left(-\nabla p + \rho_f \boldsymbol{g}\right) \cdot \frac{\hat{\boldsymbol{w}}_f}{\rho_f} \geq 0,
\end{aligned}
\tag{36}
$$

where $\boldsymbol{\chi} = -\rho^s \partial \hat{\psi}_s / \partial \boldsymbol{\xi}^p$ is a vector of stress-like plastic internal variables conjugate to $\boldsymbol{\xi}^p$.

The first line in Equation 36 after $\mathcal{D}$ is a reduced version of $\Phi_M^s$, which implies the maximum plastic dissipation principle. Therefore, the Terzaghi effective stress $\boldsymbol{\sigma}' = \boldsymbol{\sigma} + p\mathbf{1}$ should be used in the plastic yield function $f(\boldsymbol{\sigma}', \boldsymbol{\chi}) \leq 0$ and flow rule.[11] This highlights the non-uniqueness of effective stress in poromechanics.[63] In fact, experiments have revealed that the initial part of yield leading to failure is caused by the destruction of the pore structure,[51] rather than the elastic deformation of the solid grain.

The second line in Equation 36 is related to gas adsorption. If we can specify the expression of $\hat{\psi}_{\mathrm{surf}}$ as a function of $\epsilon^{ad}$, the above equation would give a constitutive law for $\epsilon^{ad}$. Similarly, the rate of adsorption by mass $\hat{r}$ should be related to the mass-specific fluid Gibbs potential $\hat{g}_f$ and interface Helmholtz free energy $\hat{\psi}_{\mathrm{surf}}$. In fact, this term with $\hat{r}$ is very similar to (3.109) in Coussy[54] for double porosity media, in which $\hat{g}_f - \hat{\psi}_{\mathrm{surf}}$ is replaced by the pressure difference between the two continua (micro-fracture network and nanoporous matrix).[44,54,56] Nevertheless, we cannot give the specific form of $\hat{\psi}_{\mathrm{surf}}$ at this moment. Therefore, it is reasonable to use alternative **empirical** relations that are also used in other reservoir geomechanics studies,[36,58] which bypasses these yet undetermined constitutive relations. More details will be given in Section 3.

The third line in Equation 36 is related to the seepage constitutive law, by assuming a linear form for $\hat{\boldsymbol{w}}_f$ with a positive definite permeability tensor, the positiveness of $\Phi_f$ will be automatically satisfied. Nevertheless, the determination of the permeability for gas flow in sedimentary rocks is not trivial, which will also be discussed in Section 3.

## 3 | CONSTITUTIVE RELATIONS

## 3.1 | Gas adsorption

As mentioned in Section 2.6, in this section, we specify the empirical constitutive laws for $\epsilon^{ad}$ and $\hat{r}$. Firstly, for $\epsilon^{ad}$, the Langmuir monolayer adsorption model (Langmuir isotherm) is adopted,[64] which gives

$$\epsilon_{ij}^{ad} = \frac{\epsilon_L p}{3(P_L + p)}\delta_{ij}, \tag{37}$$

where $\epsilon_L$ is a constant representing the maximum sorption-induced volumetric strain, which is a function of surface area, and $P_L$ is the Langmuir pressure. Note we assume $\epsilon^{ad}$ is isotropic and exclude the hysteresis effect, though we fully acknowledge that the adsorption process could be different in the bed-normal and bed-parallel directions for a transversely isotropic rock.[49,65,66]

Secondly, for $\hat{r}$, two specific forms are adopted in this study. The first one is widely used in reservoir engineering and reservoir geomechanics,[36,58,67,68] which is given as

$$m_{ad}^{(1)} = \rho_r(J - \phi_L)\frac{M_{\text{gas}}}{V_{\text{m,std}}}\frac{pV_L}{p + P_L}, \quad J\hat{r}^{(1)} = \frac{dm_{ad}^{(1)}}{dt}, \tag{38}$$

where $\rho_r \approx \rho_s$ is the rock density, $M_{\text{gas}}$ is the gas molar mass, $V_{\text{m,std}} = 22.4$ L/mol is the gas molar volume at the standard temperature and pressure (STP) condition, $V_L$ is the Langmuir volume, and $P_L$ is the same Langmuir pressure as Equation 37. The second one is derived in Zhang[49] and copied here

$$m_{ad}^{(2)} = M_{\text{gas}}\bar{A}_s \underbrace{\frac{\Gamma_{\text{gas}}^{\max} B_{\text{gas}} p}{1 + B_{\text{gas}} p}}_{\text{Surf. concentration}}, \quad \bar{A}_s = \frac{3}{R_I}\phi_0^{1/3}\phi_L^{2/3}, \quad J\hat{r}^{(2)} = \frac{dm_{ad}^{(2)}}{dt}, \tag{39}$$

where $R_I$ is the micro-structure parameter, $\Gamma_{\text{gas}}^{\max}$ and $B_{\text{gas}}$ are adsorption parameters. It should be emphasized that the adsorption process is actually a surface process, and the amount of adsorbed gas should be proportional to the surface area. From this perspective, Equation 39 appears to be a superior selection. However, given that Equation 38 is a well-established and extensively utilized formula, its existence undoubtedly holds significance. We remark that the Langmuir volume $V_L$ could contain information on micro-pore surface area,[67] thus the consistency with Equation 39 is guaranteed. In addition, as $\hat{r}^{(1)}$ is undoubtedly suitable for undeformable porous media, it should be approximately applicable when the porosity change is small for deformable porous media. More importantly, by tuning $R_I$, $\Gamma_{\text{gas}}^{\max}$, and $B_{\text{gas}}$, we could have a fair match between $m_{ad}^{(1)}$ and $m_{ad}^{(2)}$, for both elastic and plastic cases, as shown in Section 5, together with a thorough discussion on gas production.

## 3.2 | Apparent permeability model

The linear form for mass flux $\hat{\boldsymbol{w}}_f$ emanated from Equation 36 is described in detail here. We define the Darcy velocity $\boldsymbol{q}$ as $\boldsymbol{q} = \hat{\boldsymbol{w}}_f/\rho_f$. According to the non-Darcy flow of shale gas, $\boldsymbol{q}$ can be calculated through the following formula

$$\boldsymbol{q} = -\frac{k_a}{\mu_g}\nabla p. \tag{40}$$

where $k_a$ is the apparent permeability scalar and $\mu_g$ is the gas viscosity. Note we only consider isotropic permeability in this study, the idea of anisotropic permeability combined with non-Darcy flow[69] seems to be contradictory with the physical meaning of pore radius, which is not covered in this study. In order to calculate the apparent permeability $k_a$, we need to first introduce the concepts of the effective radius $r_e$ and the Knudsen number $K_n$. The effective radius $r_e$ is calculated as[36]

$$r_e = r - d_m\frac{p}{P_L + p}, \tag{41}$$

where $r$ is the current (deformed) pore radius due to a change of the porosity $\phi$ whose formula is given in the following Equation 43, $d_m = 4 \times 10^{-10}$ m is the gas molecule diameter, $P_L$ is the same Langmuir pressure as Equations 37, 38. In this work, we adopt the Kozeny-Carman equation to update the matrix intrinsic permeability $k_\infty$ as

$$k_\infty = k_0\left(\frac{\phi}{\phi_0}\right)^3\left(\frac{1 - \phi_0}{1 - \phi}\right)^2, \tag{42}$$

where $k_0$ is the initial matrix intrinsic permeability, $\phi_0$ is the initial porosity, and $\phi$ is evaluated from Equation 31. Then we use $k_\infty$ to back-calculate $r$ as

$$r = 2\sqrt{2\tau}\sqrt{\frac{k_\infty}{\phi}} = 2\sqrt{2\tau}\frac{1-\phi_0}{\phi_0}\frac{\phi}{1-\phi}\sqrt{\frac{k_0}{\phi_0}}, \tag{43}$$

where $\tau$ is the tortuosity. The Knudsen number $K_n$ is defined as the ratio of the molecular mean free path $\lambda$ to the characteristic length $r_e$ (some papers use $2r_e$ as the characteristic length)

$$K_n = \frac{\lambda}{r_e} = \frac{k_B T}{\sqrt{2}\,\pi\,d_m^2\,p\,r_e}, \tag{44}$$

where $k_B = 1.380649 \times 10^{-23}$ J/K is the Boltzmann constant and $T$ is the model temperature. The magnitude of the Knudsen number determines different regimes of gas flow. Now we can give the expression for $k_a$ [36,70,71]

$$k_a = \frac{r_e^2}{8}\frac{\phi}{\tau}(1 + \alpha_K K_n)\left(1 + \frac{4K_n}{1+K_n}\right), \tag{45}$$

where $\alpha_K$ is known as the gas rarefaction factor given as [36,72]

$$\alpha_K = \frac{128}{15\pi^2}\arctan\left(4K_n^{0.4}\right). \tag{46}$$

Although $k_a$ is suitable for most non-Darcy flow scenarios, in the case of extremely small pore radius and low gas pressure, Equation 45 would still underestimate the overall gas flow capacity. In that case, the surface diffusion is dominant. Therefore, a more complete version of apparent permeability should include surface diffusion, which is always denoted as $k_{sd}$. According to Song et al. [33] and Sun et al., [73] $k_{sd}$ adopts the following expression

$$k_{sd} = \frac{\mu_g M_{\text{gas}} D_s C_{\max}}{\rho_f}\frac{d\theta_g}{dp}\left[1 - \left(\frac{r_e}{r}\right)^2\right], \tag{47}$$

where $\theta_g$ is known as the gas coverage that is defined in an exact Langmuir-type functional relationship $\theta_g = p/(p + P_L)$, which implies that Equation 41 can also be expressed as $r_e = r - d_m\theta_g$, $C_{\max}$ is the maximum adsorbed gas concentration (mol/m$^3$), and $D_s$ is the surface diffusion coefficient (m$^2$/s). In the earlier work, $D_s$ is assumed to be a constant, [27] while in the more recent work such as Song et al. [33] and Sun et al., [73] $D_s$ is a dynamic function of $\theta_g$, as shown in the following equation

$$D_s = D_{s0}\frac{(1-\theta_g) + \frac{\kappa}{2}\theta_g(2-\theta_g) + \left\{H(1-\kappa)\right\}(1-\kappa)\frac{\kappa}{2}\theta_g^2}{\left(1 - \theta_g + \frac{\kappa}{2}\theta_g\right)^2}, \tag{48}$$

where $D_{s0}$ is the surface diffusion coefficient when gas coverage is zero (i.e., $\theta_g = 0$), $H(1-\kappa)$ is the Heaviside step function, and $\kappa$ is the ratio of the rate constant for the blockage to the rate constant for forward migration (dimensionless).

In the following numerical analysis, we will always explicitly state whether our permeability model includes $k_{sd}$.

## 3.3 | Anisotropic elastoplasticity

As the final part of this constitutive section, we need to specify the solid constitutive model. While the maximum plastic dissipation leads to the associative flow rule for plastic flow and associative hardening, for rocks, however, neither the flow rule nor hardening is associative. In this study, we review a recently developed rate-independent anisotropic plasticity model, [10,15] and demonstrate how to incorporate $\bar{\sigma}$, $\sigma'$, and $\epsilon^{ad}$.

For a transversely isotropic material where the unit normal vector to the bedding plane is $\boldsymbol{n}$, we define the microstructure tensor as $\boldsymbol{M} = \boldsymbol{n} \otimes \boldsymbol{n}$. Using this microstructure tensor, we can express $\mathbb{C}^e$ in the tensorial form in terms of five constants, which are detailed in Zhang and Borja. [9] These constants are: $E_v$ and $E_h$, which are Young's moduli in the vertical ($v$) and horizontal ($h$) directions; $\nu_{hh}$, $\nu_{vh}$, and $\nu_{hv}$, which are Poisson's ratios; and $G_{vh}$, which is the shear modulus. These

constants are directly measurable in laboratory experiments. Note that Poisson's ratios $\nu_{hv}$ and $\nu_{vh}$ are not independent and are correlated through the equation[74]

$$\frac{\nu_{vh}}{E_v} = \frac{\nu_{hv}}{E_h} . \tag{49}$$

For a transversely isotropic material with positive elastic moduli ($E_h, E_v > 0$) to be stable, the following inequality must be satisfied, as suggested by Ip et al.[75]

$$1 - \nu_{hh} > 2\nu_{vh}^2 \frac{E_h}{E_v} . \tag{50}$$

For isotropic material, Equation 50 gives $-1 < \nu < 0.5$.

As mentioned earlier, the plasticity model is now expressed in terms of the Terzaghi effective stress $\boldsymbol{\sigma}'$, which reminds us to rewrite the elastic relation $\bar{\boldsymbol{\sigma}} = \mathbb{C}^e : \boldsymbol{\epsilon}^e$ in terms of $\boldsymbol{\sigma}'$. The result reads

$$\boldsymbol{\sigma}' = \mathbb{C}^e : (\tilde{\boldsymbol{\epsilon}} - \boldsymbol{\epsilon}^p), \qquad \tilde{\boldsymbol{\epsilon}} = (\boldsymbol{\epsilon} - \boldsymbol{\epsilon}^{ad}) + (\mathbb{C}^e)^{-1} : (\mathbf{1} - \boldsymbol{\alpha})p = (\boldsymbol{\epsilon} - \boldsymbol{\epsilon}^{ad}) + \frac{p\mathbf{1}}{3K_s} , \tag{51}$$

where $\tilde{\boldsymbol{\epsilon}}$ is known as the alternative strain tensor field. The plasticity model for the solid skeleton can thus be formulated in terms of the pair ($\boldsymbol{\sigma}', \tilde{\boldsymbol{\epsilon}}$) alone.[11] To construct the anisotropic yield surface for a transversely isotropic material based on existing yield criteria, we first define a rank-four projection tensor $\mathbb{P}$ (with major and minor symmetries) to map the stress tensor $\boldsymbol{\sigma}'$ into a fictitious stress configuration $\boldsymbol{\sigma}^* = \mathbb{P} : \boldsymbol{\sigma}'$. The projection tensor is given by the following equation[76]

$$\mathbb{P} = c_1\mathbb{I} + c_2\boldsymbol{M} \odot \boldsymbol{M} + \frac{c_3}{2}(\boldsymbol{M} \odot \mathbf{1} + \mathbf{1} \odot \boldsymbol{M}), \tag{52}$$

where $c_1$, $c_2$, and $c_3$ are the anisotropy parameters, $\mathbb{I}$ is the symmetric fourth-order identity tensor, and the tensorial "$\odot$" operator is defined as $(\boldsymbol{A} \odot \boldsymbol{B})_{ijkl} = (A_{ik}B_{jl} + A_{il}B_{jk})/2$. With the fictitious and real configurations, we now define the anisotropic yield surface as

$$f = \frac{q^{*2}}{M^2} + p'(p' - p_c) \leq 0, \tag{53}$$

where $p' = \mathrm{Tr}(\boldsymbol{\sigma}')/3$, $p^* = \mathrm{Tr}(\boldsymbol{\sigma}^*)/3$, $q^* = \sqrt{3/2}\|\boldsymbol{s}^*\|$, $\boldsymbol{s}^* = \boldsymbol{\sigma}^* - p^*\mathbf{1}$, $M$ is the slope of the critical state line, and $p_c < 0$ is the preconsolidation pressure. The associative flow rule is given by the equation in the incremental form

$$\Delta\boldsymbol{\epsilon}^p = \Delta\tilde{\boldsymbol{\epsilon}}^p = \Delta\lambda\frac{\partial f}{\partial\boldsymbol{\sigma}'} , \tag{54}$$

where $\Delta\lambda$ is the plastic multiplier, and the phenomenological hardening law is given by the exponential function[77]

$$p_c = p_{c0} \exp\left(-\frac{\epsilon_v^p}{\lambda^p}\right), \tag{55}$$

where $p_{c0} < 0$ is the initial preconsolidation pressure, $\lambda^p > 0$ is the plastic compressibility parameter, and $\epsilon_v^p$ is the plastic volumetric strain. The return mapping algorithm takes the usual form: Given $\tilde{\boldsymbol{\epsilon}}$, find $\boldsymbol{\sigma}'$. Details of the numerical implementation and derivation of the algorithmic consistent tangent operator can be found in Zhang[76] and Zhao et al.[10]

# 4 | STRESS-POINT SIMULATION OF THE APPARENT PERMEABILITY

In this section, we conduct the stress-point simulation to investigate the evolution of apparent permeability $k_a$ and clarify the effects of various parameters. Different from the traditional parametric analysis of shale gas apparent permeability,[33] in which only one factor could be changed at a time, the stress-point simulation efficiently takes the element deformation into consideration[10,15] without solving the actual boundary value problem. In other words, it allows the simultaneous consideration of changes in gas pressure $p$ and porosity $\phi$.
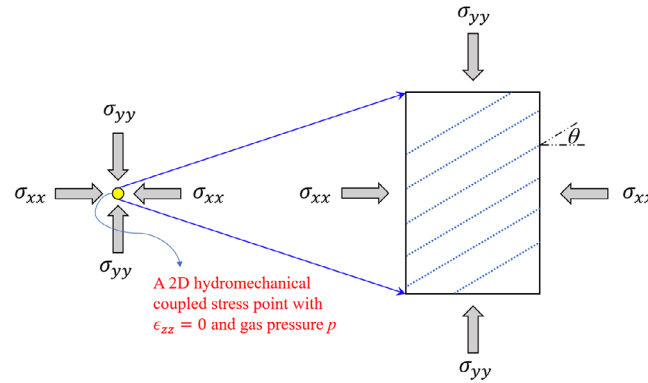
**FIGURE 1**  Schematic of the stress point simulation. $\sigma_{xx}$ and $\sigma_{yy}$ are the total horizontal and vertical stresses, respectively. This is equivalent to a representative elementary volume (REV) with uniform deformation.

Table C.1 summarizes simulation parameters for the reference case, in which some parameters will be changed later for the sensitivity analysis. Note the form of $\hat{r}$ in Section 3.1 is not necessary for the stress-point simulation. The values of moduli are consistent with the reported values in literature,[7,30,78,79] which are categorized as soft shale.[80] Three different types of point simulation are possible: strain-driven, stress-driven, and hybrid-driven. In our setting, we prescribe the total horizontal and vertical stresses $\sigma_{xx}$ and $\sigma_{yy}$, respectively, as shown in Figure 1. Next, the gas pressure decays from the initial value to the final bottom-hole pressure (BHP), and at each pressure level, we calculate the corresponding strain variation from the previous pressure level through Newton's method. However, since we assume $\epsilon_{zz} = 0$ (plane strain condition), the total stress $\sigma_{zz}$ is unknown, which makes this point simulation a hybrid-driven problem. In addition, due to the incorporation of an alternative strain $\tilde{\epsilon}$ in Equation 51, special attention must be paid to the $z$-component. Therefore, the algorithm is not trivial and should be carefully designed, as shown in Box 1.

## 4.1 | Impacts of elastoplastic parameters and surface diffusion

Firstly, we investigate the impact of elastoplastic parameters, as most of these parameters did not appear in the existing $k_a$ models, so it would be meaningful to see their influences. The results are discussed in the next few figures. For these results, $k_{sd}$ is not considered. As seen from Figure 2, an obvious transition point on the curve of $k_a$ implies that the stress state has reached the yield surface and plastic deformation accumulates. The larger the $\lambda^p$, the more pore spaces are compressed (plastic compression), which could dominate the decrease of $k_a$ for the middle stage. When the gas pressure is close to BHP, the impact of gas slippage is more significant due to a large Knudsen number $K_n$. As a result, three out of four curves increase in the final stage. While if we further increase $\lambda^p$ to 0.07, the curve of $k_a$ monotonically decreases due to a dramatic decrease in porosity, which cannot be offset by non-Darcy flow mechanisms.

Figure 3 investigates the impact of preconsolidation pressure, and it indicates that the change of $p_{c0}$ alters the transition point. For elastic deformation, the blue curve is quite similar to *fig. 2* of Yang et al.,[81] which indicates the robustness of the porosity evolution model Equation 31. It is also worthwhile to mention that the blue curves of Figure 2 and Figure 3 are in fact different since the former contains plastic deformation. Their similar values of $k_a$ is attributed to the fact that the value of $d\phi/dp$ in the plastic region does not deviate a lot from that in the elastic region.

We also investigate the impact of $\mathbb{C}^e$ and anisotropy denoted by the bedding plane orientation $\theta$ (or equivalently, $\mathbf{n}$). The results are shown in Figure 4 and Figure 5, respectively. As displayed by Figure 4, $|\mathbb{C}^e|$ controls the compression of pore spaces in both elastic and plastic stages, and a hard material enhances the non-Darcy flow effect.[81] Figure 5 suggests that $\mathbf{n}$ affects the transition point, and for one given gas pressure, $\theta = \pi/2$ predicts the highest $k_a$ and $\theta = 0$ predicts the lowest $k_a$. However, in the elastic stage, a change in $\theta$ does not affect the value of $k_a$ at all, which may not be expected from one's intuition.

Now we include $k_{sd}$ in the evaluation of apparent permeability and redo the above parametric analysis. Figure 6 and Figure 7 replot the results. Surprisingly, the evident differences among different curves in Figure 2 to Figure 5 almost disappear by adding $k_{sd}$. What is more noteworthy is that the brown and black curves may go beyond the blue curve when

**Box 1: Stress-point simulation algorithm for apparent permeability**

**Step 1**. Calculate the following quantities from the given current gas pressure $p$ and the previous gas pressure $p_n = p - \Delta p$ (in this simulation, $\Delta p$ is negative)

$$\mathbf{T}_{ext} = \begin{pmatrix} \sigma_{xx} + p \\ \sigma_{yy} + p \\ 0 \end{pmatrix}; \qquad \Delta\tilde{\epsilon}_{zz} = \frac{\Delta p}{3K_s} - \epsilon_{zz}^{ad}(p) + \epsilon_{zz}^{ad}(p_n).$$

**Step 2**. The old stress fields $\sigma'_{xx}$, $\sigma'_{yy}$, and $\sigma'_{zz}$ are known (other stress components are zero). Initialize the iteration counter $(v) = (0)$ and the initial guess $\Delta\tilde{\epsilon}_{xx}^{(0)}, \Delta\tilde{\epsilon}_{yy}^{(0)}, \Delta\tilde{\epsilon}_{xy}^{(0)} = 0$. Please note that $\Delta\tilde{\epsilon}_{xz}$ and $\Delta\tilde{\epsilon}_{yz}$ are always zero throughout the whole simulation.

**Step 3**. From $\Delta\tilde{\epsilon}^{(v)}$ and the old stress $\mathring{\sigma}'$, the solid constitutive model would predict a temporary stress $^{(v)}\sigma'$ and temporary tangent operator $\mathbb{c}^{(v)}$ through the return mapping function. The $\mathbb{c}^{(v)}$ is given as a $6 \times 6$ square matrix, while strain and stress are stored as $6 \times 1$ column vectors. This is known as the 3D Voigt notation. However, in the next step, we only need a $3 \times 3$ sub-matrix of $\mathbb{c}^{(v)}$ that corresponds to $xx$, $yy$, and $xy$ components. This sub-matrix is denoted as $\mathbb{c}_{sub}^{(v)}$.

**Step 4**. Construct the residual vector $\mathbf{r}^{(v)}$ and update $\Delta\tilde{\epsilon}^{(v)}$ to $\Delta\tilde{\epsilon}^{(v+1)}$ as ($\Delta\tilde{\epsilon}_{zz}$ is fixed as shown in Step 1, all the other components $\Delta\tilde{\epsilon}_{xz}$ and $\Delta\tilde{\epsilon}_{yz}$ remain zero)

$$\mathbf{r}^{(v)} = \begin{Bmatrix} ^{(v)}\sigma'_{xx} \\ ^{(v)}\sigma'_{yy} \\ ^{(v)}\sigma'_{xy} \end{Bmatrix} - \mathbf{T}_{ext}; \qquad \begin{Bmatrix} \Delta\tilde{\epsilon}_{xx}^{(v+1)} \\ \Delta\tilde{\epsilon}_{yy}^{(v+1)} \\ 2\Delta\tilde{\epsilon}_{xy}^{(v+1)} \end{Bmatrix} = \begin{Bmatrix} \Delta\tilde{\epsilon}_{xx}^{(v)} \\ \Delta\tilde{\epsilon}_{yy}^{(v)} \\ 2\Delta\tilde{\epsilon}_{xy}^{(v)} \end{Bmatrix} - \left[\mathbb{c}_{sub}^{(v)}\right]^{-1}\mathbf{r}^{(v)}.$$

**Step 5**. Assign $v \leftarrow v + 1$ and return to Step 3 until the norm of $\mathbf{r}^{(v)}$ is below the tolerance value. From the converged stress $\sigma'$, old stress $\mathring{\sigma}'$, and converged $\Delta\tilde{\epsilon}$ (the iteration counter $(v)$ is omitted here), the elastic strain increment and plastic strain increment could be calculated as $\Delta\epsilon^e = [C^e]^{-1}(\sigma' - \mathring{\sigma}') - \Delta p\hat{1}/(3K_s)$, $\Delta\epsilon^p = \Delta\tilde{\epsilon} - [C^e]^{-1}(\sigma' - \mathring{\sigma}')$ where $C^e$ is the $6 \times 6$ elastic stiffness matrix and $\hat{1}$ is the 3D Voigt form of the second-order identity tensor $\mathbf{1}$. Note that the increment of $\epsilon^{ad}$ can be calculated directly from Equation 37.

**Step 6**. Calculate $\phi$ from Equation 31 using the elastic strain increment $\Delta\epsilon^e$, plastic strain increment $\Delta\epsilon^p$, and adsorption strain increment $\Delta\epsilon^{ad}$. The equations in Section 3.2 can be applied now to calculate $k_a$ (briefly speaking, $\phi \Rightarrow r \Rightarrow r_e \Rightarrow K_n \Rightarrow k_a$).

**Step 7**. Assign $\mathring{\sigma}' \leftarrow \sigma'$ and $p_n \leftarrow p$, acquire the new current gas pressure $p$, and return to Step 1 until reaching BHP.

$p$ is close to BHP, as shown by Figure 6(A) and Figure 7(B). This is because, at that pressure level, a small ratio of $r_e/r$ (i.e., $d_m\theta_g$ is comparable to $r$) gives a large $k_{sd}$ from Equation 47, while for other higher pressure levels, we have $d_m\theta_g \ll r$ and $k_{sd} \approx 0$. Figure 8 suggests the same conclusion for $\epsilon_L$.

## 4.2 | Pattern in experimental permeability data

Having figured out the impact of various parameters, we now try to use this apparent permeability model to explain the experimental permeability data. We do not choose data with extremely low gas pressure, as then the curve should monotonically increase with decreasing pressure,[73] failing to highlight our model's advantage. Here we use the data from Wei et al.,[82] in which a triaxial holder was utilized for measuring coal permeability and the test gas was Helium (no adsorption and surface diffusion). The axial direction of the cylindrical coal sample was constrained to have zero displacement, and
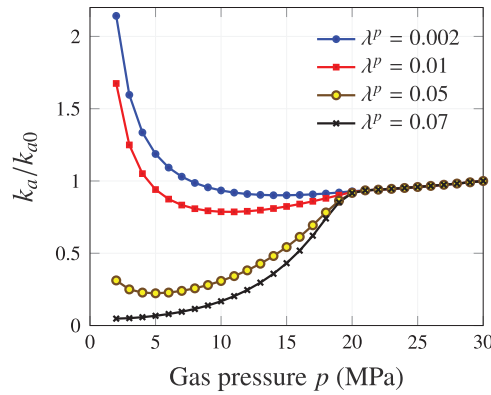
**FIGURE 2**    Variation of the normalized apparent permeability $k_a$ with gas pressure $p$ for different values of $\lambda^p$, while $p_{c0}$ and $\theta$ are kept constant at -20 MPa and $\pi/4$, respectively.
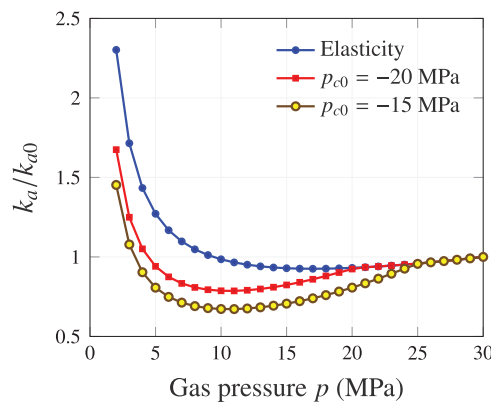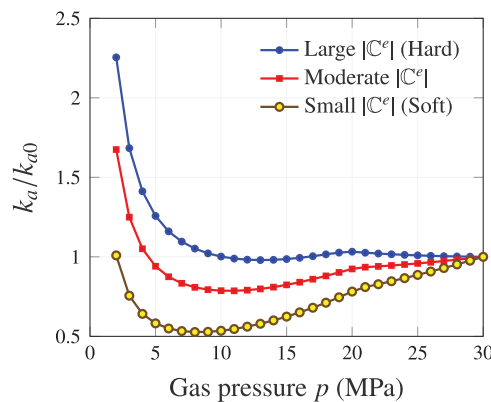
**FIGURE 3**    Variation of the normalized apparent permeability $k_a$ with gas pressure $p$ for different values of $p_{c0}$, while $\lambda^p$ and $\theta$ are kept constant at 0.01 and $\pi/4$, respectively.

**FIGURE 4**    Variation of the normalized apparent permeability $k_a$ with gas pressure $p$ for different values of $\mathbb{C}^e$, while $p_{c0}$, $\lambda^p$, and $\theta$ are kept constant at -20 MPa, 0.01, and $\pi/4$, respectively. In the figure legend, a large $|\mathbb{C}^e|$ implies a multiplication of $E_v$, $E_h$, and $G_{vh}$ by 3, while a small $|\mathbb{C}^e|$ implies a division of 2.

the circumferential boundary was subjected to compression through the use of a pump,[82] thus the previously designed algorithm applies. Since some parameters are not given in the original publication such as the bulk mechanical properties, they are tuned to match the pattern in the experimental data, which are given in Table C.2. The comparison result is given in Figure 9. It is noticeable that our model gives a better agreement with the experimental data, compared with the original numerical model by Wei et al.[82] The mechanisms behind this pattern can be summarized as follows: the
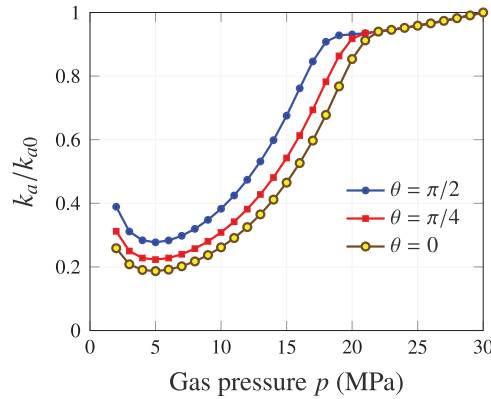
**FIGURE 5** Variation of the normalized apparent permeability $k_a$ with gas pressure $p$ for different values of bedding plane orientation $\theta$ (or equivalently, $\boldsymbol{n}$), while $\lambda^p$ and $p_{c0}$ are kept constant at 0.05 and -20 MPa, respectively.
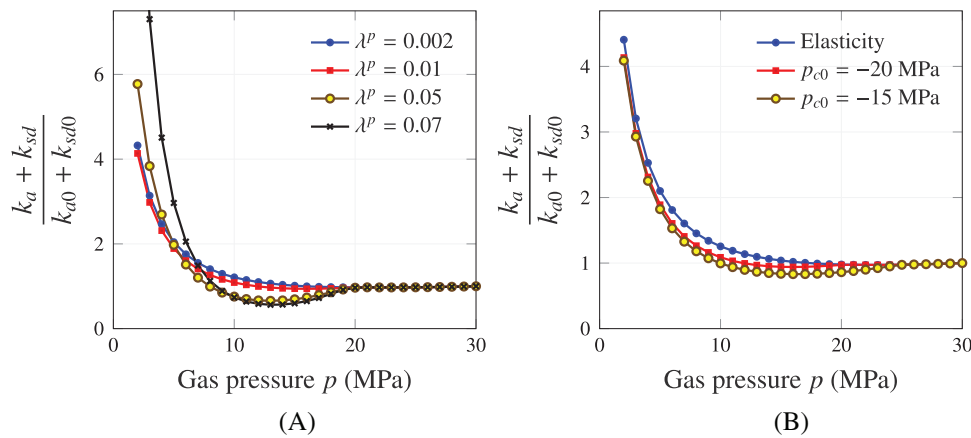


(A)



(B)

**FIGURE 6** Impact of $\lambda^p$ and $p_{c0}$ on normalized apparent permeability $k_a + k_{sd}$ with *surface diffusion*. Parameter settings can be found in Figure 2 and Figure 3.

non-Darcy effect of $k_a$ is not very strong during the elastic deformation, while the material yield causes a decline in $k_a$ as we further decrease gas pressure (a material yield could happen in this range, that is, several megapascals, see Zhao and Borja[11]), but finally, when the gas pressure is extremely low, $k_a$ increases again due to a strong non-Darcy effect. This type of curve has not been reported in any of the previous publications related to numerical apparent permeability models.

## 5 | NUMERICAL EXAMPLE OF GAS PRODUCTION

### 5.1 | Model setup

The proposed framework in Section 2 and Section 3 fits nicely into the finite element formulation,[83] with solid displacement $\boldsymbol{u}$ and gas pressure $p$ as the primary unknowns. Here, we implement this problem in a slightly different finite element framework known as the smoothed finite element method (S-FEM)[18,84,85] with equal order interpolation for $\boldsymbol{u}$ and $p$. For this numerical example, we want to focus our discussion on the influence of the elastoplasticity and adsorption model on gas production. The computational domain is of size 2 m × 2 m (plane strain, no gravity), with a well at the center of the domain (Dirichlet boundary for both $\boldsymbol{u}$ and $p$: $\boldsymbol{u} = \boldsymbol{0}$ and $p$ = BHP). The well radius is 0.1 m. We choose this geometry size to better capture the dynamics near the well since a fine mesh is required near the well, similar to those in Cao et al.[72] and Zhang et al.[86] We think for the field scale, our findings are still applicable.[87] Tractions are applied at the outer boundary as $\sigma_{xx} = -35$ MPa and $\sigma_{yy} = -40$ MPa. The finite element mesh information of the problem is given in
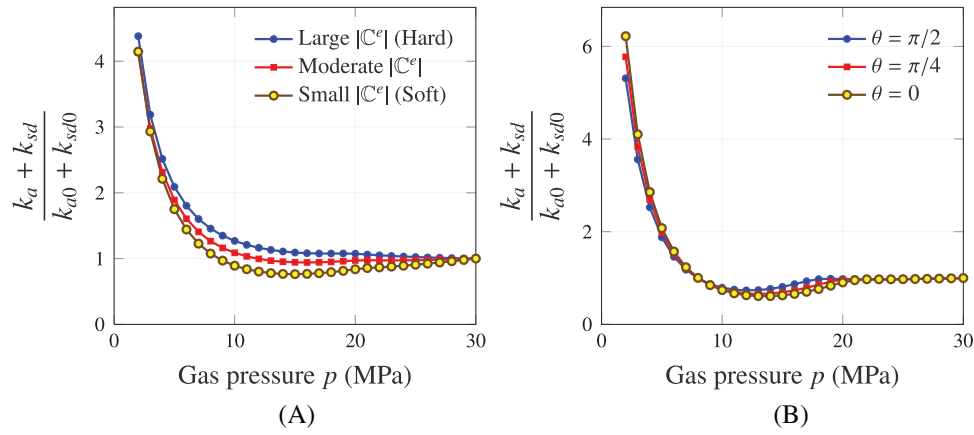
**FIGURE 7** Impact of $\mathbb{C}^e$ and $\theta$ on normalized apparent permeability $k_a + k_{sd}$ with *surface diffusion*. Parameter settings can be found in Figure 4 and Figure 5.



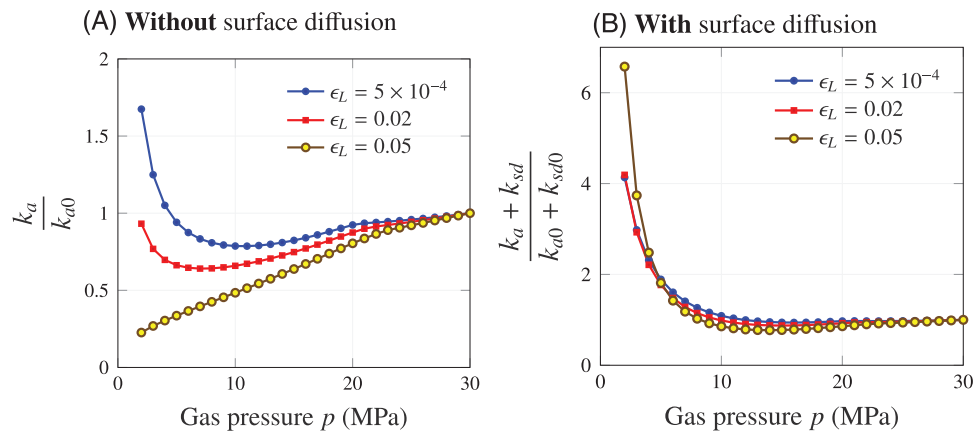**FIGURE 8** Variation of the normalized apparent permeability with gas pressure $p$ for different values of $\epsilon_L$, while $P_L$, $p_{c0}$, $\lambda^p$, and $\theta$ are kept constant at 4 MPa, -20 MPa, 0.01, and $\pi/4$, respectively.
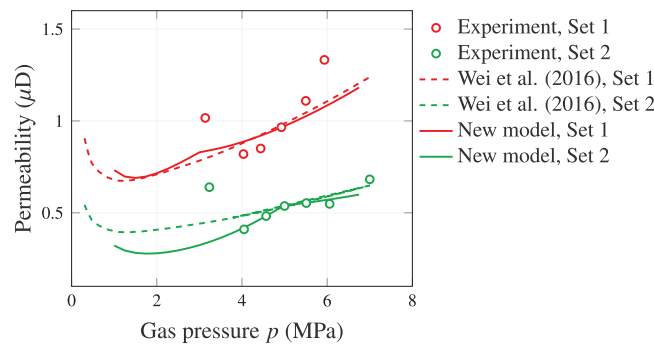


**FIGURE 9** Validation with coal sample permeability measurements.[82] A good match with experimental data is achieved by tuning parameters in the proposed model.

Figure 10. The simulation parameters are based on Table C.1 with $\lambda^p$ changed to 0.05 and $\theta = \pi/6$. $k_{sd}$ is included in the apparent permeability. In addition, more parameters from Section 3.1 need to be specified, as the point simulation does not use these parameters. Since we have two specific forms of $\hat{r}$, their parameters are given in the following bullet form.

- For $\hat{r}^{(1)}$, we have $\rho_r = 2500$ kg/m$^3$, $M_{\text{gas}} = 16.04$ g/mol, $V_L = 0.015$ m$^3$/kg, and $P_L = 4$ MPa. Note some parameters are also mentioned in Table C.1.
- For $\hat{r}^{(2)}$, we have $R_I = 15$ nm, $\phi_0 = 0.06$, $\Gamma_{\text{gas}}^{\text{max}} = 1.3 \times 10^{-4}$ mol/m$^2$, and $B_{\text{gas}} = 0.3$.
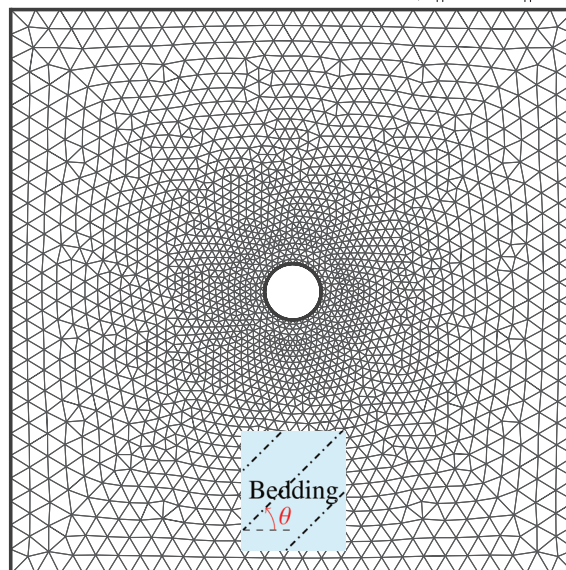
MESH-OPT.: KIND=DELFRONT, ||TRIA||=4362



**FIGURE 10**    Finite element mesh generation of the gas production problem. We have a total of 2249 nodes and 4362 triangle elements.
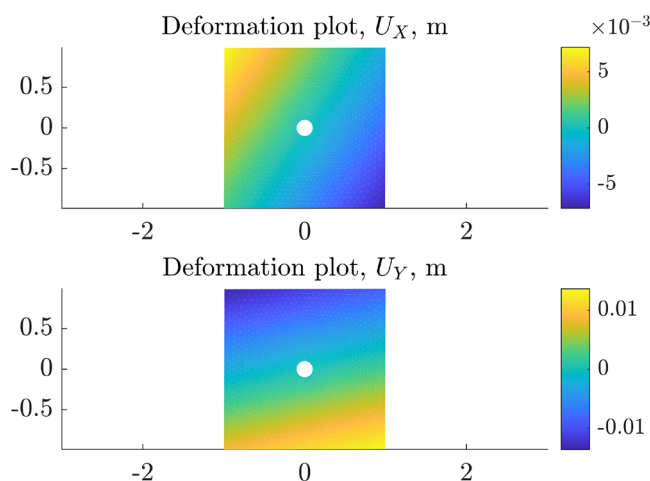


**FIGURE 11**    The horizontal and vertical displacement fields at the end of Step 40 (66.6 days) for a small-scale gas production problem. Both displacement contours are asymmetric with respect to the center well.

For the simulation time step setting, a total of 55 steps cover a time range of 500 days. Let $\Delta t_k$ represent the time increment of $k^{th}$ step, we have $\Delta t_{1\sim10} = 10$ s, $\Delta t_k = 1.5\Delta t_{k-1}$ for $k = 11, \dots, 40$, $\Delta t_{41\sim54} = 30$ d, and $\Delta t_{55}$ is calculated based on the total time range of 500 days.

The simulation is performed on the "ASUS TUF Gaming F15 Laptop" in the "Performance" mode. The Memory is 32 GB DDR4, the CPU is 13th Gen Intel(R) Core(TM) i7-13700H, and the GPU is NVIDIA GeForce RTX 4060 GDDR6 @ 8GB. The whole simulation takes about 20 min on this laptop.

## 5.2 | Model results

We initially present the cloud plot of displacement, stress, gas pressure, and equivalent plastic strain at a specific time slot (66.6 days) utilizing the adsorption model $\hat{r}^{(1)}$. As illustrated by Figure 11, the numerical model accurately captures the inclined displacement contours due to a bedding plane orientation of $\theta = \pi/6$. The vertical displacement contour is approximately parallel to the bedding plane. From the cloud plot of horizontal displacement, it is observed that the block
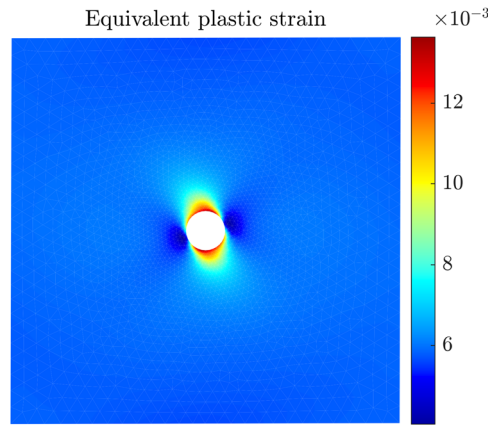
**FIGURE 12** The equivalent plastic strain $\sqrt{2/3}\|\epsilon^p\|$ field at the end of Step 40 (66.6 days) for a small-scale gas production problem. The global maximum and minimum $\|\epsilon^p\|$ all occur near the wellbore, one in the bed-normal direction, and the other in the bed-parallel direction.
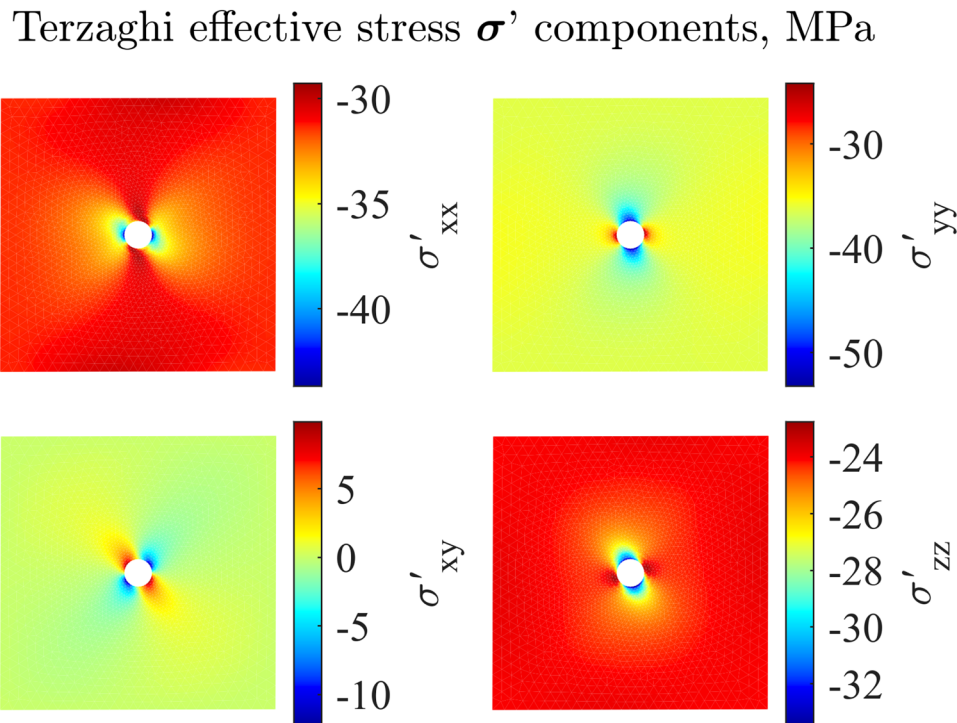


**FIGURE 13** The Terzaghi effective stress field at the end of Step 40 (66.6 days) for a small-scale gas production problem. All the stress components' distributions are affected by the bedding plane orientation.

swings to the right, aligning with the findings in Zhao et al.[10] Consequently, localized plastic zones (large $\|\epsilon^p\|$) develop, originating from the wellbore and propagating in the weaker bed-normal direction, as corroborated by Figure 12. At this moment, the entire block undergoes plastic deformation, and due to the constraint at the wellbore, the global minimum of $\|\epsilon^p\|$ also occurs near the wellbore in the bed-parallel direction. The Terzaghi effective stress field is depicted in Figure 13, revealing that the bedding plane contributes to the re-orientation of the stress distribution, and the pattern of $\sigma'_{xx}$ appears more complex than others. However, the solid anisotropy scarcely impacts the gas pressure distribution, as demonstrated by Figure 14. This is a distinctive feature of gas, in contrast to the nearly incompressible fluid.[11] Throughout the production process, the primary "driving force" is gas compressibility, not the compression of pore spaces. Moreover, from Equation 4, $J\nabla \cdot \hat{\boldsymbol{w}}_f$ would result in an additional $J\nabla\rho_f \cdot \boldsymbol{q}$ term, which is typically disregarded for the nearly incompressible fluid. Consequently, the main pressure drop is more concentrated around the wellbore.
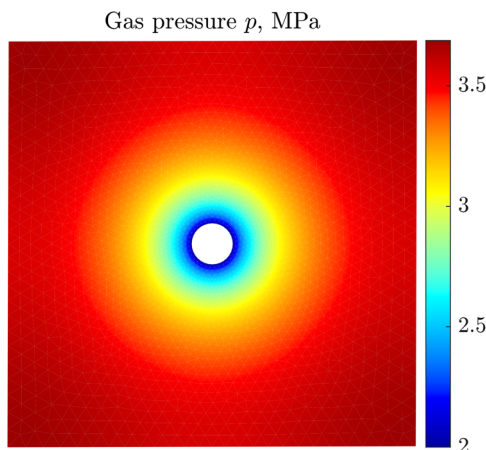
**FIGURE 14** The gas pressure field at the end of Step 40 (66.6 days) for a small-scale gas production problem. In contrast to the other fields, the gas pressure contours are still symmetric with respect to the center well.
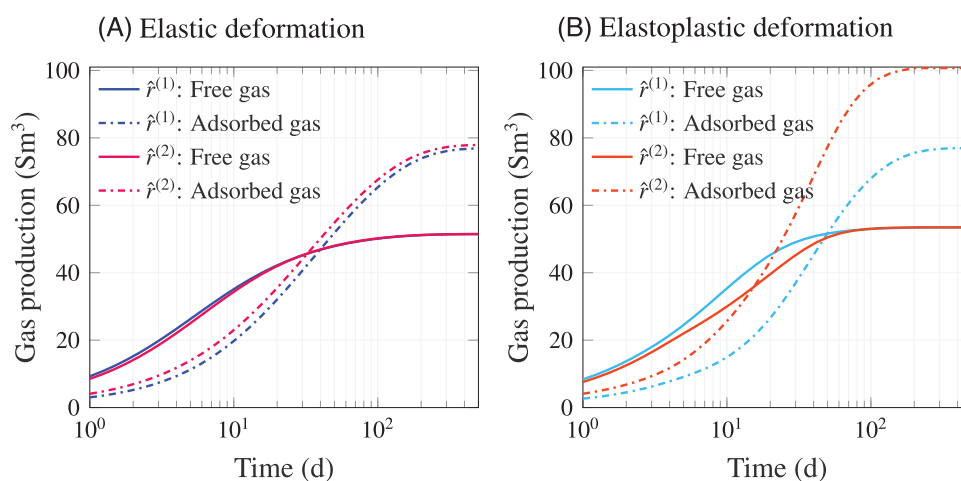


**FIGURE 15** Impact of adsorption models $\hat{r}^{(1)}$ and $\hat{r}^{(2)}$ on the cumulative gas production. Two adsorption models yield similar outcomes under elasticity (shown on the left), in contrast to the obvious differences under elastoplasticity (shown on the right). The axis label $Sm^3$ represents the gas volume in $m^3$ at the standard condition.

Next, we explore the impacts of $\hat{r}^{(1)}$ and $\hat{r}^{(2)}$ through the cumulative gas production curve and pressure decay curve at the corner point. We take into account both the elastic deformation (by adjusting $p_{c0}$ to -200 MPa) and plastic deformation. The comparative results are displayed in Figures 15, 16. For elasticity, we observe that the two adsorption models yield similar outcomes, as we have adjusted the model parameters such that $m_{ad}^{(1)}(p) \approx m_{ad}^{(2)}(p)$ in the point simulation, see Figure 17(A). However, for plasticity, the aforementioned result does not consistently hold, and findings suggest that $\hat{r}^{(2)}$ would expedite the transport of adsorbed gas. This can be discerned from Figure 15(B): the time scale difference between the release of the adsorbed gas and the release of the free gas diminishes when we employ $\hat{r}^{(2)}$. We would explain this behavior from the curve of $m_{ad}^{(2)}$ with gas pressure $p$ (adsorption isotherm) in the point simulation, as shown by Figure 17(B): the curve gets steeper when $p$ drops below the transition point, indicating that the release of the adsorbed gas would rapidly increase. This significant change of slope originates from the porosity $\phi_L$ evolution with $p$ under elastoplasticity.

For pressure dissipation in Figure 16, both $\hat{r}^{(1)}$ and $\hat{r}^{(2)}$ would lead to the "double-shell" characteristic[20,44] in gas pressure decay curve under plastic deformation, while the elastic deformation would lead to a perfect "S-shaped" curve.

## 5.3 | Summary

One of the key strengths of our work is the novel incorporation of anisotropic elastoplasticity into the gas permeability model and small-scale gas production problem, which, to the best of our knowledge, has not been done before. Through
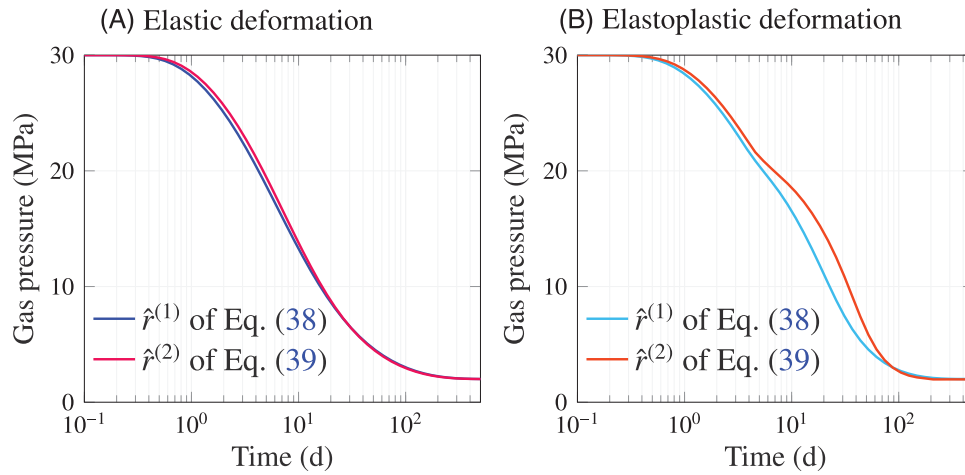
**FIGURE 16** Impact of adsorption models $\hat{r}^{(1)}$ and $\hat{r}^{(2)}$ on the pressure decay at the corner point. The "double-shell" characteristic is shown on the right, in contrast to the perfect "S-shape" shown on the left.
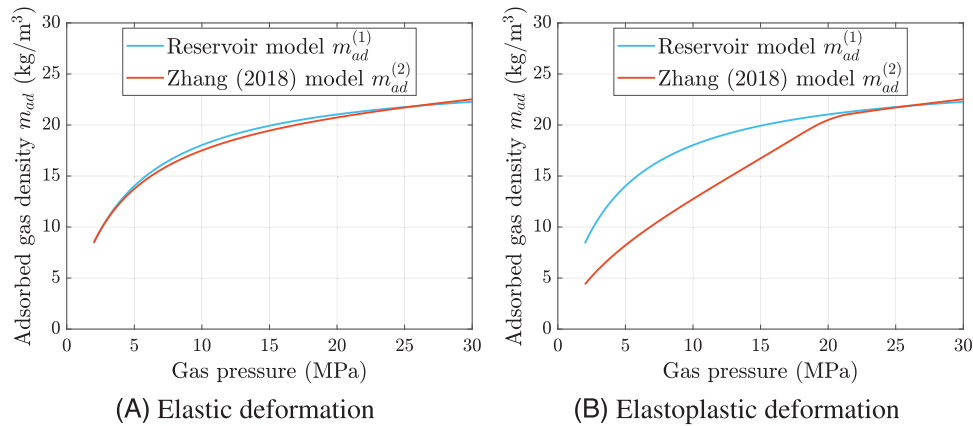


**FIGURE 17** Adsorption isotherm for two adsorption models that can be used to explain the behavior in Figure 15. We assume $\phi_L$ is obtained from the stress-point simulation in Section 4 with $\lambda^p$ changed to 0.05 and $\theta = \pi/6$, which is then substituted into Equations 38, 39.

the solution, we could observe the new apparent permeability patterns and production behaviors especially when the gas adsorption depends on the porosity.[49] However, we also recognize certain limitations. For instance, our model operates under the isothermal assumption, which may not accurately reflect reality as gas behavior is sensitive to temperature. Additionally, our model only considers single-phase gas, while in actual underground reservoirs, the flow is typically multi-phase. Furthermore, our study still relies on empirical adsorption formulas, and we acknowledge that more work needs to be done on the free energy side, such as the second line of Equation 36. We will strive to address these limitations in our future work.

## 6 | CLOSURE

An anisotropic poromechanics framework is introduced into gas flow modeling by utilizing mixture theory and continuum principles of thermodynamics, enabling us to derive novel governing equations for mass, momentum, and energy balance in sedimentary rocks with significant gas adsorption. The resulting porosity evolution equation is shown to be identical to the one derived from the phenomenological poroelasticity theory under the conditions of isotropic elastic deformation and $\epsilon_{ad} = \phi\epsilon_{ad}^p$, thereby confirming the validity of both approaches. As two effective stress measures and adsorption strain emerge from the formulation, a novel stress-point simulation algorithm is developed to update porosity and permeability. Through the stress-point simulation, we demonstrate that the overall evolution of the apparent permeability depends on

the competition among three factors: gas slippage, surface diffusion, and porosity change. The former two factors can accelerate the gas flow capacity, while the last factor generally plays the opposite role. Under specific combinations of plasticity parameters, new patterns of apparent permeability could be generated, and they are more consistent with the experimental data. We believe the apparent permeability model proposed here could provide a more accurate evaluation of tight gas reservoirs. An initial-boundary value problem of gas production is carried out to highlight the role of the bedding plane, the importance of gas compressibility, and the significance of adsorption models.

## CONFLICT OF INTEREST STATEMENT

The authors declare that they have no known competing financial interests or personal relationships that could have appeared to influence the work reported in this paper.

## DATA AVAILABILITY STATEMENT

The data that support the findings of this study are available from the following Github repository (**GasHM** folder): https://github.com/qizhang94/GEOKEYFEM_HM.

## ORCID

*Zhen-Yu Yin* https://orcid.org/0000-0003-4154-7304

## REFERENCES

1. Khadem B, Saberi MR, Avseth P. Rock physics of sand-shale mixtures: Classifications, theoretical formulations and study on real dataset. *Mar Pet Geol.* 2021;134:105366. doi:10.1016/j.marpetgeo.2021.105366
2. Li T, Han D, Yang F, et al. Modeling study of the thermal-hydraulic-mechanical coupling process for EGS based on the framework of EDFM and XFEM. *Geothermics.* 2021;89:101953. doi:10.1016/j.geothermics.2020.101953
3. Vilarrasa V, Bolster D, Olivella S, Carrera J. Coupled hydromechanical modeling of CO2 sequestration in deep saline aquifers. *Int J Greenhouse Gas Control.* 2010;4 (6):910-919. doi:10.1016/j.ijggc.2010.06.006
4. Zeng Q, Yao J, Shao J. An extended finite element solution for hydraulic fracturing with thermo-hydro-elastic–plastic coupling. *Comput Meth Appl Mech Eng.* 2020;364:112967. doi:10.1016/j.cma.2020.112967
5. Wang Z, Zhang Q, Zhang W. A novel collaborative study of abnormal roof water inrush in coal seam mining based on strata separation and wing crack initiation. *Eng Fail Anal.* 2022;142:106762. doi:10.1016/j.engfailanal.2022.106762
6. Lu S-F, Feng S-J. Coupled bio-hydro-thermo-mechanical interactions of landfilled MSW based on a multi-phase, multi-component numerical model. *Comput Geotech.* 2022;144:104659. doi:10.1016/j.compgeo.2022.104659
7. Niandou H, Shao J, Henry J, Fourmaintraux D. Laboratory investigation of the mechanical behaviour of Tournemire shale. *Int J Rock Mech Min Sci.* 1997;34 (1):3-16. doi:10.1016/S1365-1609(97)80029-9
8. Tariq MH, Ren J. General solution and Green's function for fluid-saturated infinite and semi-infinite orthotropic poro-thermoelastic materials. *Eur J Mech A Solids.* 2023;97:104816. doi:10.1016/j.euromechsol.2022.104816
9. Zhang Q, Borja RI. Poroelastic coefficients for anisotropic single and double porosity media. *Acta Geotech.* 2021;16 (10):3013-3025. doi:10.1007/s11440-021-01184-y
10. Zhao Y, Semnani SJ, Yin Q, Borja RI. On the strength of transversely isotropic rocks. *Int J Numer Anal Methods Geomech.* 2018;42 (16):1917-1934. doi:10.1002/nag.2809
11. Zhao Y, Borja RI. A continuum framework for coupled solid deformation–fluid flow through anisotropic elastoplastic porous media. *Comput Meth Appl Mech Eng.* 2020;369:113225. doi:10.1016/j.cma.2020.113225
12. Borja RI, Yin Q, Zhao Y. Cam-Clay plasticity. Part IX: On the anisotropy, heterogeneity, and viscoplasticity of shale. *Comput Meth Appl Mech Eng.* 2020;360:112695. doi:10.1016/j.cma.2019.112695
13. Choo J, Semnani SJ, White JA. An anisotropic viscoplasticity model for shale based on layered microstructure homogenization. *Int J Numer Anal Methods Geomech.* 2021;45 (4):502-520. doi:10.1002/nag.3167
14. Crook AJ, Yu J-G, Willson SM. Development of an orthotropic 3D elastoplastic material model for shale. In: SPE/ISRM Rock Mechanics Conference. 2002: pp. SPE–78238–MS. doi:10.2118/78238-MS

15. Semnani SJ, White JA, Borja RI. Thermoplasticity and strain localization in transversely isotropic materials based on anisotropic critical state plasticity. *Int J Numer Anal Methods Geomech*. 2016;40 (18):2423-2449. doi:10.1002/nag.2536

16. Zhao Y, Lai Y, Zhang J, Bai R. A bounding surface model for frozen sulfate saline silty clay considering rotation of principal stress axes. *Int J Mech Sci*. 2020;177:105570. doi:10.1016/j.ijmecsci.2020.105570

17. Zhao Y, Wang R, Zhang J-M. A dual-mechanism tensile failure criterion for transversely isotropic rocks. *Acta Geotech*. 2022;17(11):5187-5200. doi:10.1007/s11440-022-01604-7

18. Wang Z-Y, Jin Y-F, Yin Z-Y, Wang Y-Z. A novel coupled NS-PFEM with stable nodal integration and polynomial pressure projection for geotechnical problems. *Int J Numer Anal Methods Geomech*. 2022;46(13):2535-2560. doi:10.1002/nag.3417

19. Jin Y-F, Yin Z-Y. Two-phase PFEM with stable nodal integration for large deformation hydromechanical coupled geotechnical problems. *Comput Meth Appl Mech Eng*. 2022;392:114660. doi:10.1016/j.cma.2022.114660

20. Zhang Q, Yan X, Shao J. Fluid flow through anisotropic and deformable double porosity media with ultra-low matrix permeability: a continuum framework. *J Pet Sci Eng*. 2021;200:108349. doi:10.1016/j.petrol.2021.108349

21. Rezaee R. *Fundamentals of Gas Shale Reservoirs*. John Wiley & Sons, Inc; 2015. doi:10.1002/9781119039228

22. Wang X, Sheng JJ. Effect of low-velocity non-Darcy flow on well production performance in shale and tight oil reservoirs. *Fuel*. 2017;190:41-46. doi:10.1016/j.fuel.2016.11.040

23. Xiong Y, Yu J, Sun H, Yuan J, Huang Z, Wu Y-s. A New non-Darcy flow model for low-velocity multiphase flow in tight reservoirs. *Transp Porous Media*. 2017;117 (3):367-383. doi:10.1007/s11242-017-0838-8

24. Diwu P, Liu T, You Z, Jiang B, Zhou J. Effect of low velocity non-Darcy flow on pressure response in shale and tight oil reservoirs. *Fuel*. 2018;216:398-406. doi:10.1016/j.fuel.2017.11.041

25. Zeng B, Cheng L, Li C. Low velocity non-linear flow in ultra-low permeability reservoir. *J Pet Sci Eng*. 2011;80 (1):1-6. doi:10.1016/j.petrol.2011.10.006

26. Hansbo S. Aspects of vertical drain design: Darcian or non-Darcian flow. *Géotechnique*. 1997;47(5):983-992. doi:10.1680/geot.1997.47.5.983

27. Zhao J, Li Z, Hu Y, Ren L, Tao Z. The impacts of microcosmic flow in nanoscale shale matrix pores on the gas production of a hydraulically fractured shale-gas well. *J Nat Gas Sci Eng*. 2016;29:431-439. doi:10.1016/j.jngse.2016.01.025

28. Zhang Q, Su Y, Wang W, Lu M, Sheng G. Gas transport behaviors in shale nanopores based on multiple mechanisms and macroscale modeling. *Int J Heat Mass Transfer*. 2018;125:845-857. doi:10.1016/j.ijheatmasstransfer.2018.04.129

29. Javadpour F, Fisher D, Unsworth M. Nanoscale gas flow in shale gas sediments. *J Can Pet Technol*. 2007;46 (10):55-61. doi:10.2118/07-10-06

30. Zhao Y, Lu G, Zhang L, Wei Y, Guo J, Chang C. Numerical simulation of shale gas reservoirs considering discrete fracture network using a coupled multiple transport mechanisms and geomechanics model. *J Pet Sci Eng*. 2020b;195:107588. doi:10.1016/j.petrol.2020.107588

31. Guo C, Xu J, Wu K, Wei M, Liu S. Study on gas flow through nano pores of shale gas reservoirs. *Fuel*. 2015;143:107-117. doi:10.1016/j.fuel.2014.11.032

32. Singh H, Javadpour F, Ettehadtavakkol A, Darabi H. Nonempirical apparent permeability of shale. *SPE Reservoir Eval Eng*. 2014;17 (03):414-424. doi:10.2118/170243-PA

33. Song W, Yao J, Li Y, et al. Apparent gas permeability in an organic-rich shale reservoir. *Fuel*. 2016;181:973-984. doi:10.1016/j.fuel.2016.05.011

34. Beskok A, Karniadakis GE. A model for flows in channels, pipes, and ducts at micro and nano scales. *Microscale Thermophys Eng*. 1999;3 (1):43-77. doi:10.1080/108939599199864

35. Brochard L, Vandamme M, Pellenq R-M. Poromechanics of microporous media. *J Mech Phys Solids*. 2012;60 (4):606-622. doi:10.1016/j.jmps.2012.01.001

36. Jiang J, Yang J. Coupled fluid flow and geomechanics modeling of stress-sensitive production behavior in fractured shale gas reservoirs. *Int J Rock Mech Min Sci*. 2018;101:1-12. doi:10.1016/j.ijrmms.2017.11.003

37. Hatami M, Bayless D, Sarvestani A. Poroelastic effects on gas transport mechanisms and influence on apparent permeability in shale. *Int J Rock Mech Min Sci*. 2022;153:105102. doi:10.1016/j.ijrmms.2022.105102

38. Belhaj HA. Dynamic modeling of tight unconventional reservoirs. In: *Tight Oil Reservoirs*. Elsevier; 2023:157-210. doi:10.1016/B978-0-12-820269-2.00003-2

39. Civan F. Effective correlation of apparent gas permeability in tight porous media. *Transp Porous Media*. 2010;82 (2):375-384. doi:10.1007/s11242-009-9432-z

40. Wang H, Chen L, Qu Z, et al. Modeling of multi-scale transport phenomena in shale gas production – a critical review. *Appl Energy*. 2020;262:114575. doi:10.1016/j.apenergy.2020.114575

41. Ip SCY, Borja RI. Multiscale interactions of elastic anisotropy in unsaturated clayey rocks using a homogenization model. *Acta Geotech*. 2023;18 (5):2289-2307. doi:10.1007/s11440-022-01784-2

42. Ma L, Fauchille A-L, Dowey PJ, et al. Correlative multi-scale imaging of shales: a review and future perspectives. Geological Society, London, Special Publications; 2017;454(1):175-199. doi:10.1144/SP454.11

43. Zhang Q, Yan X, Li Z. A mathematical framework for multiphase poromechanics in multiple porosity media. *Comput Geotech*. 2022b;146:104728. doi:10.1016/j.compgeo.2022.104728

44. Zhao Y, Borja RI. Anisotropic elastoplastic response of double-porosity media. *Comput Meth Appl Mech Eng*. 2021;380:113797. doi:10.1016/j.cma.2021.113797

45. Auton LC, MacMinn CW. Large poroelasto-plastic deformations due to radially outward fluid injection. *J Mech Phys Solids*. 2019;132:103690. doi:10.1016/j.jmps.2019.103690

46. Zheng P, Zhang K. On the effective stress law and its application to finite deformation problems in a poroelastic solid. *Int J Mech Sci.* 2019;161-162:105074. doi:10.1016/j.ijmecsci.2019.105074

47. Coussy O, Dormieux L, Detournay E. From mixture theory to biot's approach for porous media. *Int J Solids Struct.* 1998;35(34-35):4619-4635. doi:10.1016/S0020-7683(98)00087-0

48. Borja RI. On the mechanical energy and effective stress in saturated and unsaturated porous continua. *Int J Solids Struct.* 2006;43 (6):1764-1786. doi:10.1016/j.ijsolstr.2005.04.045

49. Zhang Y. Mechanics of adsorption-deformation coupling in porous media. *J Mech Phys Solids.* 2018;114:31-54. doi:10.1016/j.jmps.2018.02.009

50. Karrech A, Poulet T, Regenauer-Lieb K. Poromechanics of saturated media based on the logarithmic finite strain. *Mech Mater.* 2012;51:118-136. doi:10.1016/j.mechmat.2012.03.011

51. Cheng AHD. Intrinsic material constants of poroelasticity. *Int J Rock Mech Min Sci.* 2021;142:104754. doi:10.1016/j.ijrmms.2021.104754

52. Choo J, Borja RI. Stabilized mixed finite elements for deformable porous media with double porosity. *Comput Meth Appl Mech Eng.* 2015;293:131-154. doi:10.1016/j.cma.2015.03.023

53. Choo J, White JA, Borja RI. Hydromechanical modeling of unsaturated flow in double porosity media. *Int J Geomech.* 2016;16(6):D4016002. doi:10.1061/(ASCE)GM.1943-5622.0000558

54. Coussy O. *Poromechanics.* John Wiley & Sons Ltd; 2003. doi:10.1002/0470092718

55. Holzapfel GA. *Nonlinear Solid Mechanics: A Continuum Approach for Engineering.* John Wiley & Sons Ltd; 2000.

56. Zhang Q, Choo J, Borja RI. On the preferential flow patterns induced by transverse isotropy and non-Darcy flow in double porosity media. *Comput Meth Appl Mech Eng.* 2019;353:570-592. doi:10.1016/j.cma.2019.04.037

57. Shi JQ, Durucan S. Drawdown induced changes in permeability of coalbeds: a new interpretation of the reservoir response to primary recovery. *Transp Porous Media.* 2004;56 (1):1-16. doi:10.1023/B:TIPM.0000018398.19928.5a

58. Huang J, Ghassemi A. A poroelastic model for evolution of fractured reservoirs during gas production. *J Pet Sci Eng.* 2015;135:626-644. doi:10.1016/j.petrol.2015.10.007

59. Cheng AHD. *Poroelasticity.* Springer Science; 2016. doi:10.1007/978-3-319-25202-5

60. Zhang W, Mehrabian A. Coupled poromechanics and adsorption in multiple-porosity solids. *Physical Mesomechanics.* 2023;26(4):402-414. doi:10.1134/S1029959923040033

61. Espinoza D, Vandamme M, Pereira J-M, Dangla P, Vidal-Gilbert S. Measurement and modeling of adsorptive–poromechanical properties of bituminous coal cores exposed to CO2: adsorption, swelling strains, swelling stresses and impact on fracture permeability. *Int J Coal Geol.* 2014;134-135:80-95. doi:10.1016/j.coal.2014.09.010

62. Vandamme M, Brochard L, Lecampion B, Coussy O. Adsorption and strain: the CO2-induced swelling of coal. *J Mech Phys Solids.* 2010;58 (10):1489-1505. doi:10.1016/j.jmps.2010.07.014

63. Cheng AHD. A linear constitutive model for unsaturated poroelasticity by micromechanical analysis. *Int J Numer Anal Methods Geomech.* 2020;44 (4):455-483. doi:10.1002/nag.3033

64. Langmuir I. The constitution and fundamental properties of solids and liquids. *J Franklin Inst.* 1917;183 (1):102-105. doi:10.1016/S0016-0032(17)90938-X

65. Chen W, Zhao Y, Borja RI. Solid–fluid interaction in porous materials with internal erosion. *Acta Geotechnica.* 2023. doi:10.1007/s11440-023-01906-4

66. Ip SCY, Borja RI. Evolution of anisotropy with saturation and its implications for the elastoplastic responses of clay rocks. *Int J Numer Anal Methods Geomech.* 2022;46 (1):23-46. doi:10.1002/nag.3289

67. Yan X, Huang Z, Yao J, et al. An efficient numerical hybrid model for multiphase flow in deformable fractured-shale reservoirs. *SPE J.* 2018;23 (04):1412-1437. doi:10.2118/191122-PA

68. Saghafi A, Faiz M, Roberts D. CO2 storage and gas diffusivity properties of coals from Sydney Basin, Australia. *Int J Coal Geol.* 2007;70 (1-3):240-254. doi:10.1016/j.coal.2006.03.006

69. Huang T, Tao Z, Li E, Lyu Q, Guo X. Effect of permeability anisotropy on the production of multi-scale shale gas reservoirs. *Energies.* 2017;10 (10):1549. doi:10.3390/en10101549

70. Freeman CM, Moridis GJ, Blasingame TA. A numerical study of microscale flow behavior in tight gas and shale gas reservoir systems. *Transp Porous Media.* 2011;90 (1):253-268. doi:10.1007/s11242-011-9761-6

71. Florence FA, Rushing JA, Newsham KE, Blasingame TA. Improved permeability prediction relations for low-permeability sands. In: *Rocky Mountain Oil & Gas Technology Symposium.* SPE; 2007: pp. SPE–107954–MS. doi:10.2118/107954-MS

72. Cao P, Liu J, Leong Y-K. General gas permeability model for porous media: bridging the gaps between conventional and unconventional natural gas reservoirs. *Energy Fuels.* 2016;30(7):5492-5505. doi:10.1021/acs.energyfuels.6b00683

73. Sun Z, Shi J, Wu K, et al. Transport capacity of gas confined in nanoporous ultra-tight gas reservoirs with real gas effect and water storage mechanisms coupling. *Int J Heat Mass Transfer.* 2018;126:1007-1018. doi:10.1016/j.ijheatmasstransfer.2018.05.078

74. Liu C, Abousleiman YN. Generalized solution to the anisotropic Mandel's problem. *Int J Numer Anal Methods Geomech.* 2020;44 (17):2283-2303. doi:10.1002/nag.3128

75. Ip, SCY, Choo J, Borja RI. Impacts of saturation-dependent anisotropy on the shrinkage behavior of clay rocks. *Acta Geotech.* 2021;16 (11):3381-3400. doi:10.1007/s11440-021-01268-9

76. Zhang Q. Hydromechanical modeling of solid deformation and fluid flow in the transversely isotropic fissured rocks. *Comput Geotech.* 2020;128:103812. doi:10.1016/j.compgeo.2020.103812

77. Chen SL, Abousleiman YN. A graphical analysis-based method for undrained cylindrical cavity expansion in modified Cam Clay soil. *Géotechnique*. 2022:1-11. doi:10.1680/jgeot.21.00172

78. Rybacki E, Reinicke A, Meier T, Makasi M, Dresen G. What controls the mechanical properties of shale rocks? - Part I: Strength and Young's modulus. *J Pet Sci Eng*. 2015;135:702-722. doi:10.1016/j.petrol.2015.10.028

79. Josh M, Esteban L, Delle Piane C, Sarout J, Dewhurst D, Clennell M. Laboratory characterization of shale properties. *J Pet Sci Eng*. 2012;88-89:107-124. doi:10.1016/j.petrol.2012.01.023

80. Yu W, Sepehrnoori K. Simulation of gas desorption and geomechanics effects for unconventional gas reservoirs. *Fuel*. 2014;116:455-464. doi:10.1016/j.fuel.2013.08.032

81. Yang X, Zhang H, et al. Gas migration in the reservoirs of ultra-low porosity and permeability based on an improved apparent permeability model. *J Pet Sci Eng*. 2020;185:106614. doi:10.1016/j.petrol.2019.106614

82. Wei M, Liu J, Feng X, Wang C, Zhou F. Evolution of shale apparent permeability from stress-controlled to displacement-controlled conditions. *J Nat Gas Sci Eng*. 2016;34:1453-1460. doi:10.1016/j.jngse.2016.07.012

83. Borja RI, Chen W, Odufisan AR. A constitutive framework for rocks undergoing solid dissolution. *J Mech Phys Solids*. 2023;173:105198. doi:10.1016/j.jmps.2023.105198

84. Zhang Q, Wang Z-Y, Yin Z-Y, Jin Y-F. A novel stabilized NS-FEM formulation for anisotropic double porosity media. *Comput Meth Appl Mech Eng*. 2022;401:115666. doi:10.1016/j.cma.2022.115666

85. Liu GR, Dai KY, Nguyen TT. A smoothed finite element method for mechanics problems. *Comput Mech*. 2007;39 (6):859-877. doi:10.1007/s00466-006-0075-4

86. Zhang H, Liu J, Elsworth D. How sorption-induced matrix deformation affects gas flow in coal seams: a new FE model. *Int J Rock Mech Min Sci*. 2008;45 (8):1226-1236. doi:10.1016/j.ijrmms.2007.11.007

87. Zhang Q, Yin Z-Y, Yan X. Material constants of anisotropic poroelasticity and its impacts on shale gas production. *Energy Fuels*. 2023;37(23):18722-18734. doi:10.1021/acs.energyfuels.3c02656

88. Láng GG. Some remarks concerning the thermodynamics of the simple ideal gas and related mathematical background. *ChemTexts*. 2016;2. doi:10.1007/s40828-016-0028-2

89. Wang HF. *Theory of linear poroelasticity with applications to geomechanics and hydrogeology*. Princeton Series in Geophysics. Princeton University Press; 2000.

90. Detournay E, Cheng AH-D. Fundamentals of Poroelasticity. In: *Analysis and Design Methods*. Elsevier; 1993:113-171. doi:10.1016/B978-0-08-040615-2.50011-3

91. Cao P, Liu J, Leong Y-K. Combined impact of flow regimes and effective stress on the evolution of shale apparent permeability. *J Unconv Oil Gas Resour*. 2016;14:32-43. doi:10.1016/j.juogr.2016.01.004

---

**How to cite this article:** Zhang Q, Yin Z-Y, Yan X. Anisotropic continuum framework of coupled gas flow – adsorption – deformation in sedimentary rocks. *Int J Numer Anal Methods*. 2024;48:1018–1045. https://doi.org/10.1002/nag.3674

---

## APPENDIX A: STATE EQUATIONS FOR AN IDEAL MONOATOMIC GAS

We first convert the Gibbs potential $G(T, p, n)$ provided by Láng[88] (cf. 25b) to the dimension of per unit mass (mass-specific) by dividing $nM_{gas}$, where $n$ is the chemical amount of substance of the gas and $M_{gas}$ is the gas molar mass, the result reads

$$\hat{g}_f (p, T) = \frac{5RT}{2M_{gas}} - T(\hat{s}_f)_0 - \frac{5RT}{2M_{gas}} \ln \left( \frac{T}{T_0} \right) + \frac{RT}{M_{gas}} \ln \left( \frac{p}{p_0} \right), \tag{A.1}$$

where $(\hat{s}_f)_0$ is denoted as the reference mass-specific fluid entropy and $R$ is the gas constant. Similarly, from (22) of Láng,[88] we know

$$\hat{h}_f = \frac{5RT}{2M_{gas}}. \tag{A.2}$$

Since $\hat{g}_f = \hat{h}_f - T\hat{s}_f$, we can solve $\hat{s}_f$ from Equations A.1, A.2 as

$$\hat{s}_f = (\hat{s}_f)_0 + \frac{5R}{2M_{gas}} \ln \left( \frac{T}{T_0} \right) - \frac{R}{M_{gas}} \ln \left( \frac{p}{p_0} \right). \tag{A.3}$$

This expression for $\hat{s}_f$ is quite intuitive as the entropy would increase with a higher temperature and would decrease with a larger pressure, and it is also consistent with (4.57) in Coussy.[54] Now by using the rule of total differentiation, we can verify (note the use of ideal gas law)

$$d\hat{g}_f = \frac{\partial \hat{g}_f}{\partial p}dp + \frac{\partial \hat{g}_f}{\partial T}dT, \quad \frac{\partial \hat{g}_f}{\partial p} = \frac{RT}{pM_{\text{gas}}} = \frac{1}{\rho_f}, \quad \frac{\partial \hat{g}_f}{\partial T} = -\hat{s}_f, \tag{A.4}$$

which is exactly Equation 22.

Secondly, to verify Equation 23, we first use the relation $\hat{\psi}_f = \hat{g}_f - p/\rho_f = \hat{g}_f - RT/M_{\text{gas}}$ and express $\hat{\psi}_f$ as

$$\hat{\psi}_f = \frac{3RT}{2M_{\text{gas}}} - T(\hat{s}_f)_0 - \frac{5RT}{2M_{\text{gas}}} \ln\left(\frac{T}{T_0}\right) + \frac{RT}{M_{\text{gas}}} \ln\left(\frac{p}{p_0}\right). \tag{A.5}$$

Next, by noting that

$$\frac{p}{p_0} = \frac{\rho_f}{(\rho_f)_0} \frac{T}{T_0}, \tag{A.6}$$

Equation (A.3) could also be written as

$$\hat{s}_f = (\hat{s}_f)_0 + \frac{3R}{2M_{\text{gas}}} \ln\left(\frac{T}{T_0}\right) - \frac{R}{M_{\text{gas}}} \ln\left[\frac{1/(\rho_f)_0}{1/\rho_f}\right], \tag{A.7}$$

and $\hat{\psi}_f$ depends on $1/\rho_f$ and $T$ as

$$\hat{\psi}_f(1/\rho_f, T) = \frac{3RT}{2M_{\text{gas}}} - T(\hat{s}_f)_0 - \frac{3RT}{2M_{\text{gas}}} \ln\left(\frac{T}{T_0}\right) + \frac{RT}{M_{\text{gas}}} \ln\left[\frac{1/(\rho_f)_0}{1/\rho_f}\right]. \tag{A.8}$$

By using the rule of total differentiation, it is easy to verify that

$$d\hat{\psi}_f = \frac{\partial \hat{\psi}_f}{\partial(1/\rho_f)}d\left(\frac{1}{\rho_f}\right) + \frac{\partial \hat{\psi}_f}{\partial T}dT, \quad \frac{\partial \hat{\psi}_f}{\partial(1/\rho_f)} = -\frac{RT}{M_g \times 1/\rho_f} = -p, \quad \frac{\partial \hat{\psi}_f}{\partial T} = -\hat{s}_f, \tag{A.9}$$

which is exactly Equation 23.

## APPENDIX B: POROSITY EVOLUTION EQUATION FROM POROELASTICITY THEORY

Suppose we have a porous material with volume $V$, where the interconnected pore space has a volume of $V_p$. The porosity $\phi$ is defined as the ratio of $V_p$ to $V$. The material is subjected to a total pressure of $P$ and a pore pressure of $p$.[89] We can describe the volumetric response of the material to loading $\{P, p\}$ in terms of $\Delta V/V$, the volumetric strain of the bulk material, and $\Delta V_p/V_p$, the volumetric strain of the pore space. The linearity assumption copied from (23a)(23b) of Detournay and Cheng[90] implies (assuming that before loading, there is zero stress and pore pressure)

$$\frac{\Delta V}{V} = -\frac{P'}{K} - \frac{p}{K'_s}, \tag{B.1}$$

$$\frac{\Delta V_p}{V_p} = -\frac{P'}{K_p} - \frac{p}{K''_s}, \tag{B.2}$$

where $P' = P - p$ is the Terzaghi effective pressure, $K$ is the bulk modulus for the bulk volumetric strain, and $K_p$ is the bulk modulus for the pore volumetric strain. The coefficients $K'_s$ and $K''_s$ are two bulk moduli, which under the assumption of ideal porous media[90] can be both identified with the bulk modulus $K_s$ of the solid constituent, and this equivalence is accepted by default in the following derivations as well as in the mixture theory. $K'_s \neq K''_s$ implies the micro-heterogeneity of the material, which is not the focus of this work. Interested readers may refer to Cheng[51] and Zhang et al.[87] for more details.

Since the adsorption strain could exist in this study, we may modify Equations B.1, B.2 as

$$\frac{\Delta V}{V} = -\frac{P'}{K} - \frac{p}{K_s} + \epsilon_{ad}, \tag{B.3}$$

$$\frac{\Delta V_p}{V_p} = -\frac{P'}{K_p} - \frac{p}{K_s} + \epsilon_{ad}^p, \tag{B.4}$$

where a new parameter $\epsilon_{ad}^p$, namely, the sorption strain of the pores, has been introduced. There are some researchers that assume $\epsilon_{ad}^p = \epsilon_{ad}$,[86,91] while others suggest $\epsilon_{ad}^p = \eta \epsilon_{ad}$ and $\eta$ is generally a negative constant.[81] Note in this appendix, we use $\epsilon_{ad}$ to represent the trace of $\epsilon^{ad}$ introduced in the body text, in order to keep the notation consistency with other references for isotropic poroelasticity. By subtracting (25b) from (25a) of Detournay and Cheng,[90] we obtain an important relation

$$\frac{\Delta\phi}{\phi} = \frac{\Delta V_p}{V_p} - \frac{\Delta V}{V}. \tag{B.5}$$

Substituting Equations B.3, B.4 into Equation B.5 yields

$$\frac{\Delta\phi}{\phi} = \left(\frac{1}{K} - \frac{1}{K_p}\right)(P - p) + \left(\epsilon_{ad}^p - \epsilon_{ad}\right). \tag{B.6}$$

As long as $\epsilon_{ad}^p = \epsilon_{ad}$, it is the Terzaghi effective pressure $P'$ that controls pore structure change.[51] By invoking the Betti-Maxwell reciprocal theorem,[86,90] we obtain

$$K_p = \frac{\phi}{\alpha} K, \tag{B.7}$$

where $\alpha = 1 - (K/K_s)$ is the Biot-Wills coefficient[89] and it is identical to the Biot coefficient tensor $\boldsymbol{\alpha}$ under the assumption of isotropy. The isotropic linear elasticity constitutive law leads to the following equation

$$\epsilon_v^e = \epsilon_v - \epsilon_{ad} = -\frac{\bar{P}}{K} = -\frac{P - \alpha p}{K} \implies P - p = -K\left(\epsilon_v + \frac{p}{K_s} - \epsilon_{ad}\right), \tag{B.8}$$

where $\bar{P} = P - \alpha p$ is known as the Biot effective pressure. By using Equations B.7 and B.8 in Equation B.6, we have

$$\Delta\phi = (\alpha - \phi)\left(\epsilon_v + \frac{p}{K_s} - \epsilon_{ad}\right) + \phi\left(\epsilon_{ad}^p - \epsilon_{ad}\right). \tag{B.9}$$

As mentioned earlier, Equation B.9 is derived from the assumption of zero stress and zero pore pressure before loading, so $\Delta\phi$ can be represented as $\phi - \phi_0$, where $\phi_0$ is the initial porosity before loading. Solving $\phi$ from Equation B.9 yields (note that $\epsilon_v^e = \epsilon_v - \epsilon_{ad}$)

$$\phi = \frac{\phi_0 + \alpha\left(\epsilon_v^e + \frac{p}{K_s}\right)}{1 + \epsilon_v + \frac{p}{K_s} - \epsilon_{ad}^p}. \tag{B.10}$$

In Equation 31, by assuming a zero initial state, that is, all the quantities with subscript "n" are zero (except $\phi_n$) and $\phi_n = \phi_0$, we obtain

$$\phi = \frac{\phi_0 + \boldsymbol{\alpha} : \boldsymbol{\epsilon}^e + \epsilon_v^p + \epsilon_{ad} + \frac{(\boldsymbol{\alpha} : \mathbf{1})p}{3K_s}}{1 + \epsilon_v + \frac{p}{K_s}}, \tag{B.11}$$

A comparison between Equation B.10 and Equation B.11 indicates that two equations are identical when $\epsilon_{ad} = \phi\epsilon_{ad}^p$ and isotropic elasticity is assumed to be valid, in other words, $\epsilon_v^p \equiv 0$ and $\boldsymbol{\alpha} = \alpha\mathbf{1}$.

## APPENDIX C: TABLE OF MATERIAL PARAMETERS

**TABLE C.1** Solid and gas flow parameters of the plane strain stress-point simulation and the initial-boundary value problem.

| Parameter | Value | Unit |
|---|---|---|
| Young's modulus $E_v$[1] | 4.286 | GPa |
| Young's modulus $E_h$[1] | 7.3 | GPa |
| Poisson's ratio $\nu_{hv}$[2] | 0.15 | 1 |
| Poisson's ratio $\nu_{hh}$ in the plane of isotropy | 0.17 | 1 |
| Shear modulus $G_{vh}$[3] | 2.17 | GPa |
| Bedding plane orientation $\theta$[4] | $\pi/4$ | rad |
| Plastic anisotropy parameter $c_1$ in Equation 52 | 0.7 | 1 |
| Plastic anisotropy parameter $c_2$ in Equation 52 | -0.36 | 1 |
| Plastic anisotropy parameter $c_3$ in Equation 52 | 0.6 | 1 |
| Slope of the critical state line $M$ | 1.07 | 1 |
| Plastic compressibility parameter $\lambda^p$ | 0.01 | 1 |
| Initial preconsolidation pressure $p_{c0}$ | -20 | MPa |
| Intrinsic bulk modulus of solid $K_s$ | 30 | GPa |
| Initial matrix porosity $\phi_0$ | 0.06 | 1 |
| Initial $\sigma'_{xx}$, $\sigma'_{yy}$, and $\sigma'_{zz}$ | -5, -10, -5 | MPa |
| Total horizontal stress $\sigma_{xx}$ (constant) | -35 | MPa |
| Total vertical stress $\sigma_{yy}$ (constant) | -40 | MPa |
| Gas molar mass $M_{\text{gas}}$ | 16.04 | g/mol |
| Langmuir pressure $P_L$ | 4 | MPa |
| Model temperature $T$ | 80 | °C |
| Gas viscosity $\mu_g$ | $2 \times 10^{-5}$ | Pa·s |
| $\epsilon_L$ in sorption model | $5 \times 10^{-4}$ | 1 |
| Initial matrix intrinsic permeability $k_0$ | $2 \times 10^{-19}$ | m$^2$ |
| Tortuosity $\tau$ | 2 | 1 |
| Coefficient $D_{s0}$ under $\theta_g = 0$ | 7.09767 | mm$^2$/s |
| Maximum adsorbed gas concentration $C_{\max}$ | 328.7 | mol/m$^3$ |
| $\kappa$ in Equation 48 | 0.5 | 1 |
| Initial gas pressure | 30 | MPa |
| BHP | 2 | MPa |

[1]$E_v$ is in the bed-normal (BN) direction and $E_h$ is in the bed-parallel (BP) direction.

[2]$\nu_{hv} = \varepsilon_{e,BN}/\varepsilon_{c,BP}$: ratio of induced extension in BN to compression in BP direction.

[3]$G_{vh}$ characterizes the angular deformation between BN and BP directions.

[4]Bedding normal $\boldsymbol{n} = [-\sin\theta, \cos\theta, 0]^{\mathsf{T}}$

**TABLE C.2** Solid and gas flow parameters of the stress-point simulation for two sets of experimental data from coal sample. The remaining parameters can be found in Table C.1.

| Parameter | Data set 1 | Data set 2 | Unit |
|---|---|---|---|
| Young's modulus $E_v$ | 0.5357 | 0.7143 | GPa |
| Young's modulus $E_h$ | 0.9125 | 1.2167 | GPa |
| Shear modulus $G_{vh}$ | 0.2712 | 0.3617 | GPa |
| Bedding plane orientation $\theta$ | 0 | 0 | rad |
| Slope of the critical state line $M$ | 0.75 | 0.75 | 1 |
| Plastic compressibility parameter $\lambda^p$ | 0.03 | 0.03 | 1 |
| Initial preconsolidation pressure $p_{c0}$ | -8 | -8 | MPa |
| Intrinsic bulk modulus of solid $K_s$ | $+\infty$ | $+\infty$ | GPa |
| Initial matrix porosity $\phi_0$ | 0.05 | 0.05 | 1 |
| Total confining stress (constant) | -9 | -12 | MPa |
| Gas molar mass $M_{\text{gas}}$ (Helium) | 4 | 4 | g/mol |
| Langmuir pressure $P_L$ | $+\infty$ | $+\infty$ | MPa |
| Model temperature $T$ | 50 | 50 | °C |
| Initial nanopore radius $r_0$[1] | 22 | 15 | nm |
| Tortuosity $\tau$ | 3 | 3 | 1 |
| Initial gas pressure | 7 | 7 | MPa |
| BHP | 1 | 1 | MPa |

[1]Initial matrix intrinsic permeability $k_0 = \phi_0 r_0^2/(8\tau)$.